ÉCOLE DE TECHNOLOGIE SUPÉRIEURE
UNIVERSITÉ DU QUÉBEC

THESIS REPORT PRESENTED TO
ÉCOLE DE TECHNOLOGIE SUPÉRIEURE

SUBMITTED IN PARTIAL FULFILLMENT
OF THE REQUIREMENTS FOR THE DEGREE OF
MASTER IN CONSTRUCTION ENGINEERING

BY
MENAA MEROUANE

PERFORMANCE OF SURFACE STRUCTURES SUBJECTED TO SUBSURFACE
SOIL EROSION

MONTRÉAL, July 25th 2008

THIS THESIS WAS EVALUATED

BY A COMMITTEE MADE UP OF :

M. Gabriel Assaf, Supervisor
Department of construction engineering at École de technologie supérieure.

M. Mohamed A. Meguid, Co-Supervisor
Department of Civil Engineering and Applied Mechanics at McGill University.

M. Omar Chaallal, Chair
Department of construction engineering at École de technologie supérieure.

M. Jean-Sébastien Dubé, External examiner
 Department of construction engineering at École de technologie supérieure.

THIS THESIS WAS PRESENTED TO THE COMMITTEE AND THE ASSISTANCE

ON JULY 8th 2008

AT ÉCOLE DE TECHNOLOGIE SUPÉRIEURE

ACKNOWLEDGEMENTS

PERFORMANCE OF SURFACE STRUCTURES SUBJECTED TO SUBSURFACE SOIL EROSION

MENAA MEROUANE

ABSTRACT

Several geotechnical engineering structures (e.g. pavements, slabs-on-grade, footings) transfer pressure to the ground through a contact area with the supporting soil. Design of these structures usually assumes that full contact is established throughout the service life of the structure. Erosion of the subgrade soil is a common mechanism that can lead to the development of subsurface voids and consequently a contact loss between the structure and the supporting soil characterized by a void space under the structure.

The performance of surface structures such as concrete pavements, slabs-on-grade, and sidewalks subjected to subsurface soil erosion is investigated experimentally and numerically in this thesis. The experiments were performed in a rigid tank holding a prism of sand with artificially created soil erosion; supporting a rigid steel plate. The surface deformation and contact pressure at the plate-soil interface were measured to quantify the effect of subsurface soil erosion on the stresses developing in the surface structure. Numerical modeling was conducted using 2D elasto-plastic finite element analysis. The model was first validated using the experimental results. Several scenarios were then considered where parameters such as the volume of soil erosion, its location, and the magnitude of the load the concrete slab is subjected to, were varied. Results of this investigation indicated that when the void space is centered under the slab-on-grade, tensile stresses developing in the structure increased as the size of the void increased causing ultimately the failure of the slab. It has also been concluded that when the void is off-centered, the supporting soil around the void space is likely to experience shear failure before excessive tensile stresses develop in the outermost fibers of the structure.

Key words: subsurface soil erosion, slab-on-grade, cracking, experimental modeling, finite element analysis.

ÉTUDE DE PERFORMANCE DES STRUCTURES DE SURFACE SUJETTES A L'ÉROSION SOUS-JACENTE

MENAA MEROUANE

RÉSUMÉ

Plusieurs infrastructures géotechniques (ex. chaussées, dalles, fondations) exercent une pression à travers leurs surfaces de contact avec le sol. Le dimensionnement de ces structures suppose un contact parfait tout au long de la vie de service de celles-ci. Par ailleurs, l'érosion des sols sous-jacents est un mécanisme qui peut contribuer au développement de cavités souterraines et par conséquent à une perte locale de contact entre la structure et le sol, caractérisée par un vide sous la structure.

La performance des structures telles que les chaussées en béton, les dalles ainsi que les trottoirs sujettes à l'érosion souterraine est étudiée expérimentalement et numériquement dans ce mémoire. Les expériences ont été menées dans un caisson en acier rigide contenant du sable où l'érosion souterraine a été crée artificiellement; le tout supportant une plaque en acier rigide. Les déformations de la surface ainsi que les pressions de contact à l'interface plaque-sol ont été mesurées afin de quantifier les effets de l'érosion souterraine sur les contraintes développées dans la structure. L'étude numérique a été conduite en utilisant un modèle élastoplastique à 2 dimensions. Le modèle a été calibré avec les résultats expérimentaux et divers scénarios ont été envisagés. Des paramètres tels que le volume du sol érodé, sa localisation ainsi que les chargements appliqués sur la dalle de béton ont été variés. Les résultats de cette recherche ont montré que lorsque le vide est centré directement sous la dalle, les contraintes de traction développées dans celle-ci augmentent avec la taille du vide provoquant ainsi la rupture de la dalle. Il a également été conclu que lorsque le vide est excentré, le sol au voisinage de celui-ci est susceptible de subir une rupture avant que des contraintes de traction excessives ne se développent dans la fibre la plus tendue de la dalle en béton.

Mots clés: érosion souterraine, dalle, fissure, modélisation expérimentale, éléments finis

TABLE OF CONTENTS

LIST OF TABLES

LIST OF FIGURES

Page

LIST OF SYMBOLS

1D	One dimension
2D	Two dimensions
3D	Three dimensions
ASTM	American society for testing and material
CH	Clays of high plasticity
GPR	Ground penetrating radar
HSS	Hollow structural section
MH	Silts of high plasticity
OH	Organic clays
WRc	Water Research Center
A	Normal section
Ac	Activity factor
B	Void width
D	Void depth
D	Depth to void
E	Young modulus
E_{50}	Confining stress dependent stiffness modulus
E_{50}^{ref}	Reference stiffness modulus
E_{ur}	Elastic modulus
E_{ur}^{ref}	Reference elastic modulus
E_{oed}	Oedometer stiffness

E_{oed}^{ref}	Tangent stiffness at vertical stress
f_c	Concrete compressive strength
H	Sand surface height
I	Inertia
Ko	Coefficient of lateral earth pressure at rest
K_0^{nc}	Normally consolidated coefficient of lateral earth pressure at rest
P	Isotropic stress
P	Load
P_p	Isotropic preconsolidation stress
P_H	Dimensionless coefficient
PI	Plasticity index
R_f	Failure ratio
S	Settlement
W	Void width
W	Concrete unit weight
X	Axe of abscissa
Y	ordinate axe
Z	Depth to void
a	Area of soil tension
a	Half of footing width
c	Cohesion
d	Steel plate thickness

f	Yield function
$\overline{f}$	Function of stress
f^c	Cap yield surface
f_c	Compressive strength
g	Gravity
h	Water elevation
m	Stiffness stress dependency
p^{ref}	Reference confining pressure
q	Deviatoric stress
q_a	Asymptotic deviatoric stress
q_f	Ultimate deviatoric stress
$\tilde{q}$	Special stress measure for deviatoric stresses
r	Circular void radius
φ	Friction angle
ε_1	Axial strain
σ'_3	Minor principal stress
σ'_1	Major principal stress
γ^p	Hardening parameter
ε_1^p	Axial plastic strain
ε_v^p	Volumetric plastic strain
$\dot{\varepsilon}_v^p$	Rate of plastic volumetric strain and

$\dot{\gamma}^p$	Rate of plastic shear strain
ψ_m	Mobilized dilatancy angle
φ_{cv}	Critical friction angle
φ_m	Mobilized friction angle
β	Relative soil thickness.
α	Auxiliary parameter related to K_0^{nc}
υ	Poison ration
υ_{ur}	Poison ration in primary loading
σ_t	Tensile stresses
σ_{adm}	Admissible tensile stresses
ρ	Water unit weight

INTRODUCTION

Context of the research

Among the 100,000 kilometers of Canadian sidewalks, 15 to 20% need to be replaced. These structures are designed to last for a period of 20 to 40 years, however, in some Canadian cities, premature failure is observed 1 to 5 years after construction. Consequently, the repair or replacement costs of sidewalks assumed by Canadian municipalities are estimated to $1.5 to $2.4 billion (Rajani, 2002).

Sidewalks in North-America are essentially slab-on-grade and the most common loading they are subjected to, comes from snow removal vehicles. The observed deteriorations can take several forms i.e., rigid body movements, joint buckling/blow-up, popout, shattering, corner break, scaling, crazing, shrinkage cracks, longitudinal cracks, faulting, "D" cracks, transverse cracks, joint spalling, or corner spalling. These deteriorations are usually attributed to two main factors. The first involves aspects related to material failure, which includes fatigue of the concrete and other construction defects. The second category is attributed to the loss of reaction support. The behavior of slabs-on-grade is best understood by studying the corresponding soil-structure interaction rather than the individual aspects of the slab or the soil. In this research, the effects of subsurface soil erosion on the performance of concrete slabs directly supported on the erodable subgrade are investigated. The erosion mechanism is characterized by a soil volume loss responsible for ground deformation leading to loss of support underneath the slab. As illustrated in the figure at the end of the Introduction, the phenomenon is problematic when the partially unsupported slab-on-grade experiences deformations that induce excessive tensile stresses in the outer fibers of the concrete or when the supporting soil around the void experience excessive shear stresses.

Objectives and scope

The three main objectives of the research are listed below:

- Build a physical model that simulates one dimensional volume loss under a rigid structure according to the mechanism illustrated in the figure at the end of the Introduction.

- Monitor the physical model to measure parameters such as the surface settlement and the contact pressure at the structure-soil interface.

- Conduct 2D elasto-plastic finite element analyses to investigate (a) the structural behavior of a concrete slab-on-grade subjected to a uniform loading and a loss of support due to subsurface volume loss (b) the failure mechanism of the soil-structure system.

State of Montréal sidewalks

A survey to evaluate the condition of sidewalks at Montréal has been conducted in September 2006 with the following objectives: (a) determine the proportion of each type of cracks and the slab movements encountered based on visual observations; (b) estimate the age of the sidewalks surveyed; (c) gather as many information as possible concerning the underlying soil through boring logs. Six streets were selected for the investigation because of either the amount of structural subsidence observed (St-Laurent, St-Denis, St-Valier) or because the sidewalks seemed to be recently constructed (Mont-Royal, Sherbrooke and St-Hubert). The exact sections of the streets surveyed are listed below:

- Mont-Royal avenue between Saint-Denis and De Lorimier
- Sherbrooke street between Berri and Jeanne Mance
- Saint-Hubert street between Villier and Jean Talon

- Saint-Laurent boulevard between Mont-Royal and Rachel
- Saint-Denis street between Beaubien and Jean Talon
- Saint-Valier street between Beaubien and Saint-Zotique

The general surficial soil descriptions of the surveyed streets are described below. The complete soil boring logs gathered from the city of Montréal can be found in Appendix I. The subsurface materials of Mont-Royal avenue consists of a 0.5 m fill of clayey sand containing a small amount of rock fragments, overlying a hard or soft clay layer of variable thickness. The surficial stratigraphy of Sherbrooke street is composed of a fill containing gravels with presence of asphalt and concrete, or clayey silt with small amount of sand, or silty clay. The thickness of the fill varies from 0.5 m to 1.22 m and is usually underlain by a layer of clay with medium to high plasticity index. Only two locations were sounded for Saint-Hubert street and over a short depth. The boreholes indicated the presence of a fill layer containing sand with small amount of silt, trace of gravel, stones, blocs and various materials (charcoal, metal, asphalt). Brown silty and sandy moraine with gravels follow the fill over a depth of 2.6 m. Regarding Saint-Laurent boulevard, the borings indicate the presence of a shallow cracked limestone rock preceded by a fill of gravel, sand and small amount of silt. At some locations the stratigraphy consists of 1.7 m to 2 m layer of brown sandy clay with small amount of gravel or clayey fine sand overlying bedrock. The boreholes carried out on Saint-Denis street reveal for the most of them a layer with a thickness around 0.6 m of angular stones, sand silt and trace of clay size particles; over a shaly limestone. Saint-Valier street is generally constituted of a cracked limestone rock around 2 m depth from the surface overlain by a layer of sand, gravel and silt for an average thickness between 3 and 6 m.

The visual aspect of Mont-Royal, Sherbrooke and Saint-Hubert sidewalks indicates that they were recently constructed whereas Saint-Denis, Saint-Laurent and Saint-Valier showed significant deteriorations. All the pictures taken during this survey are classified in Appendix II. Most of the crack patterns observed are transverse followed by "D" cracks and then longitudinal cracks. The slab movement mode is essentially a rigid body movement

(Tilt, Uplift, settlement). Regarding the streets where sidewalks seem to be recently constructed, most of the cracks appear as hairlines without faulting. For the highly deteriorated streets multiple types of deterioration were observed such as popout, joint spalling, corner spalling, deterioration of the concrete at the top surface, slab completely split and crazing. Concerning St-Denis street, heavy trees are set up every five meters and the slabs are uplifted at the bottom of the trunk.

Applications

The systematical replacement of the deteriorated sidewalks during a period of budgetary restrictions is unjustified and expensive. The minimal financial effort already required for maintenance and reparations is already huge. In this context, the development of maintenance strategies that would be efficient, durable and economical represents a major challenge for the construction industry. An analogy to sewer rehabilitation is worth to be mentioned. Indeed, because of the huge amount of sewers to be rehabilitated in the UK, the water research center put in place a strategic long-term maintenance planning (WRc, 1994). This planning takes into consideration the probability that an event would happen through parameters such as the surrounding soil, the type of the pipe, the complaints registered by the municipalities, etc.; and the consequences that would be endured because of this event. Consequently, a map that represents the sewers network with a grade attributed to each section helps to prioritize the sewers to be inspected and possibly rehabilitated. Therefore, information such as the size of the void and its location beneath the slab-on-grade that induce critical stresses in the concrete or the supporting soil represent parameters that could be used to schedule strategic long-term rehabilitation planning. Actions such as identifying the size and the location of the void with non destructive techniques (i.e. Ground penetration radar) can be taken and if necessary injecting a liquid mortar into the void before the latter reaches a critical size.

Thesis organization

This thesis is divided into four chapters. The organization of these chapters reflects the methodology pursued during this research. The first chapter reviews in the first section the problems encountered during the service life of the slab-on-grade including the types of damage and the modes of deformation followed by the common construction practices. The second section discusses the main causes that lead to slab-on-grade deterioration focusing on the contribution of the supporting soil. This chapter concludes with a literature review on the soil-structure interaction when the soil is subjected to subsurface voids and the stability of underground cavities.

Chapter 3 describes how the physical model was built and discusses the results of the experimental investigation. This chapter is not restricted to the description of the final setup but explains the process that led to it.

Chapter 4 is dedicated to the numerical analysis and contains two main sections.
The first section describes the constitutive model, the strategy used to simulate the experimental tests and discusses the result of the calibration. The second section presents and discusses the full scale analyses.

Finally, the last part of the thesis contains general conclusions and suggestions for further research.
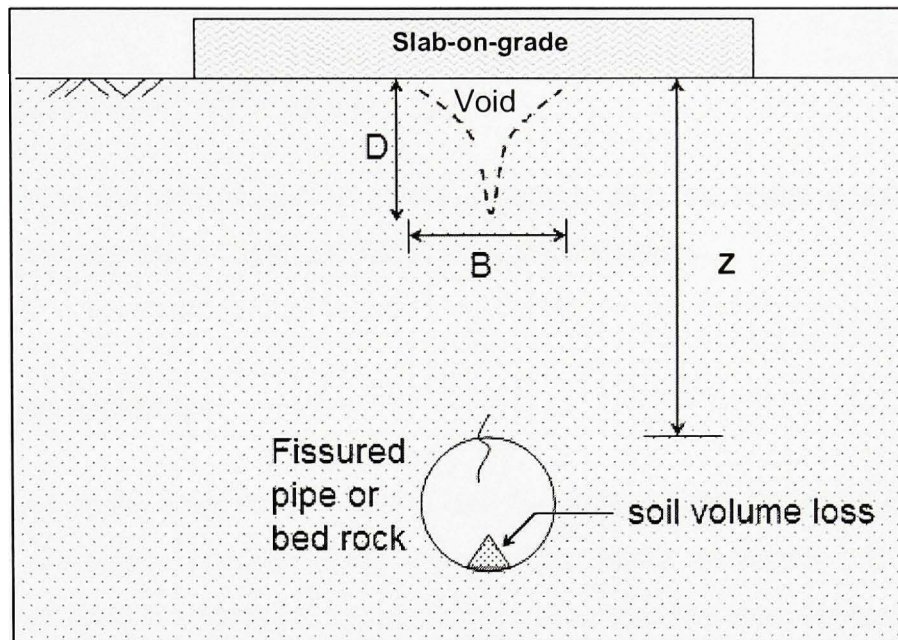
Performance of slab-on-grade subjected to subsurface soil erosion

CHAPTER 1

LITERATURE REVIEW

1.1   Performance of slab-on-grade

In this section, the performance of slabs-on-grade implies the visual symptoms mostly observed and the modes of deformation the slabs are subjected to.

1.1.1   Types of damage

The main reason for crack development in slabs-on-grade is when forces induce stresses in excess of the tensile strength of the concrete. As shown on Figure 1.1, three major categories of crack are identified (Rajani and Zhan 1997). The most encountered type of crack is the longitudinal crack that usually appears in the middle third of the slab. The cracks initially appear as hairlines, but they open up with time and faulting develops. It is worth mentioning that observations have shown that longitudinal cracks increase with the plasticity index of the subgrade, although no correlation was found between them (Rajani and Zhan 1997).

A second type of crack, the transverse crack, results from a non-uniform compaction rather than a lack of compaction. These cracks are also subjected to opening and faulting.

The third category is the "D" corner crack. Corner cracks are also a consequence of inadequate grading of the subgrade. An uplift movement of the slab may cause corner breakage resulting from friction at the control joints if the underlying soil is subjected to frost heave or shrinkage movements. Based on observations, corner crack occur in regions where longitudinal cracks are not predominant (Rajani and Zhan, 1997).

1.1.2   Mode of deformation

As shown in Figure 1.2, slabs-on-grade are usually subjected simultaneously to several modes of deformation. Deteriorations occur when these modes of deformation induce excessive tensile strains in the concrete. As described below, four major modes of deformation are identified (Rajani, 2002).

Rigid body movement which represents a uniform movement where the slab rises, subsides or tilts. This type of movement results from expansive soil, frost susceptible soil or thermal expansion of the concrete (Figure 1.2).

The two second major modes of deformation are "sagging" and "hogging" which represent a non uniform movement that leads to longitudinal cracks. It occurs when the soil is subjected to a differential settlement between the center and the edge of the slab due to a freeze/thaw or swell/shrink of the underlying soil (Figure 1.3).

The last major mode of deformation is tensile-shrinkage, which is a horizontal movement caused by a moisture decrease of the underlying soil. When an expansive soil dries, tensile stresses are induced in the concrete slab. Cracks appear when the tensile stresses induced by the underlying soil exceed the tensile strength of the concrete (Figure 1.3).

1.2   Practices of slab-on-grade construction

Concrete sidewalks are essentially slab-on-grade underlain by a first layer that constitutes the subbase and a second one that constitutes the subgrade. Each entity needs to be prepared in order to ensure long-term performance, safety and comfort.

1.2.1   Characteristics of the subgrade

The subgrade refers to the native soil underlying the slab-on-grade. The integrity of the latter is strongly related to the uniformity of the subgrade rather than its bearing capacity, because of the low pressures the soil has to support. Uniform subgrade can be improved by controlling soil expansion, frost susceptible materials and grading.

While non uniform compaction rather than the degree of compaction is responsible for corner and transversal cracks on sidewalks, it is usually assumed that longitudinal cracks increase with plasticity index (Rajani and Zhan, 1997). Soil with plasticity index over 20 may cause significant changes in moisture and consequently high soil volume change. When compaction is applied on highly expansive soil, swelling and softening can occur during subsequent wetting if the soil is too dry. If the soil is too wet, shrinkage may create instability and transmits tensile strains to the sidewalk, which is a principal cause of cracks. Compact expansive soil to 95% of the optimum density at 1% to 3% higher than the optimum moisture content provides a subgrade with the required stability (Portland Cement Association, 1983). Frost action is also responsible for deteriorations due to differential movements. It is recommended to remove frost susceptible soils and replace them with gravel material.

1.2.2   Characteristics of the subbase

The subbase is usually a layer of granular material placed between the subgrade and the slab-on-grade. Its principal role is to provide a cushion to compensate for the minor subgrade defects and reduce the development of suction which can induce problems due to frost action.

Studies carried out by the Portland Cement Association (1983) show that it is not economical to build a subbase over 101 mm thickness to improve support or diminish slab thickness. However, although uniform support rather than strong support is required from

the subbase and the subgrade, a subbase layer of 150 mm compacted to 95% of the standard proctor density is usually used in Canada.

The Portland Cement Association (1983) recommends a subbase with a dense-graded material that meets the requirements summarized in Table 1.1.

Table 1.1

Characteristics of the subbase

Material	Sand, sand-gravel, crushed stone or combinations
Maximum particle size	No more than $\frac{1}{3}$ of the subbase thickness
Passing No.200 sieve	15% maximum
Plasticity index	6 maximum
Liquid limit	25 maximum

1.2.3   Characteristics of the concrete

In Canada, concrete sidewalks are essentially slab-on-grade of 150 mm thickness. The concrete quality is mostly affected by the top 6 mm that represent the wearing surface. Thus the placeability of the concrete and the finishability of the surface are as important as the strength because of the impact they have on the sidewalk surface. The general specifications for the concrete sidewalks in Canada are (Rajani, 2002): Strength (25 to 35 MPa), minimum cement content (333 kg/m^3), maximum size of coarse particles (19 mm), slump

(50 to 100 mm) and air entrainment (5.5 to 8%). Except for sidewalks that cross a driveway entrance and are subjected to vehicle load, steel reinforcement is not required.

To better understand the behavior of the concrete slab-on-grade, a special attention must be taken to the soil-structure interaction rather than to the individual aspect of the slab or the soil characteristics.

1.2.4   Jointing the concrete

Two types of joints are used for sidewalk construction. The first type is the expansion joints (also called isolation joints) that allow for independent movements of the slab. Twelve millimeters of compressible material is recommended every 15 m along the sidewalk or when a rigid structure is encountered. The second type of joints is the control joints (also called contraction or cut joints). Their function is to relieve stresses induced thermally or by shrinkage allowing the horizontal movement of the slab. Control joints are placed transversally every 1.2 to 2 m along the sidewalk. However, longitudinal control joints are also recommended since longitudinal cracks are very frequent and can extend through several slabs, usually along the centerline.

1.2.5   Overview of the practices at the city of Montréal

Sidewalks in Montréal can be monolith or built in two parts (boulevard sidewalk). The subgrade is graded but not compacted except when the native soil is of poor quality and has to be replaced. A 20 mm layer of crushed stone compacted to 95% of the optimum modified Proctor density is then used. A layer of 150 mm thick of clean stone forms the subbase. The size of the granular material ranges from 10 to 31.5 mm (usually sold at 20 mm). Four simple passes are performed using a vibrating plate.

Regarding the concrete characteristics, a complete specification report released by the city of Montréal to the ready mixed concrete suppliers is included in Appendix III. The main characteristics are summarized in Table 1.2 below:

Table 1.2

Characteristics of the concrete

Compressive strength (MPa)	32 to 35
Minimum cement content	Specified by the supplier respecting a ratio: $\dfrac{\text{water}}{\text{cement}} < 0.45$
Maximum size of granular material (mm)	20
Slump (mm)	80 ± 30
Air content (%)	5 to 8

1.3   Causes of deterioration

The causes of sidewalk deterioration are multiple and often a combination of several mechanisms. Among theses mechanisms we can identify those relevant to quality concrete, freeze-thaw cycles and expansive soil. However, emphasis is placed in this study on the mechanism of subsurface soil erosion.

1.3.1 Subsurface soil erosion

Subsurface soil erosion is one of the contributing factors to the deterioration of surface structures such as concrete pavements, slabs-on-grade and sidewalks. Erosion of the subgrade is usually defined as a downward migration of unconsolidated deposits into bedrock openings and leads to a formation and propagation of cavities. This mechanism is responsible for surface deformation creating loss of support underneath surface structure (Sterpi, 2003), and at the extreme point the development of sinkholes.

Soil erosion is usually associated to Karst terrain (Newton, 1984). Karst refers to a distinctive terrain that evolves through dissolution of the bedrock and development of underground drainage (Waltham and Bell and Culshaw, 2005). It is therefore associated to soluble rock such as limestone, dolostone, marble, gypsum, and carbonate rock. Karst terrain possesses hydrological characteristics favorable to soil erosion as they often contain a significant number of joints that accelerate the rate of internal seepage. Surface deformation can also be attributed to a vertical upward propagation of an uneven subgrade due to bedrock weathering (Kemmerly, 1993).

The development of induced sinkholes is well documented in the literature. Although, sinkholes represent the extreme consequence of subsurface erosion, the mechanism is similar to the one responsible for the loss of support underneath surface structures and leads to their deterioration. Induced sinkhole or doline refers to those caused by man's activities and exceeds natural sinkholes occurrence in many areas (Newton and Tanner 1986). They are divided into two types (Newton 1987). The first includes those resulting from water level lowering due to pumpage and leading to (1) loss of buoyant support; (2) increase in water velocity; (3) water level fluctuations; and (4) induced recharge. The second type involves those resulting from construction such as erection of structures that induce surface loading, or diversion/drainage of water that modify the underground seepage movement. Also included is leakage from sewer and similar facilities (Giroud et al, 1990, Tharp, 1999).

1.3.2   Frost susceptible soil

Many parts of Canada are overlain by frost susceptible soil responsible for sever deteriorations to surface structure such as slabs-on-grade or pavements. Segregation and ice lenses are the main causes of these deteriorations. For instance, the pavement load-carrying capacity is strongly influenced in the freeze/thaw cycles as the pavement temperature can range from -40 °C to -50 °C and the frozen depth can reach up to 2 m (Watson and Rajapakse, 2000). As the stiffness of the granular base and the subgrade soil underlying the pavement increases during the winter, a state of near-saturation is reached in the spring season once thawing cycle take place. Pavements are thus at their weakest state during this period which significantly reduces their load-carrying capacity.

A survey program carried out by Rajani and Zhan (1997) monitored seasonal variations such as sidewalk movements, frost depth and moisture in five cities at monthly intervals over a period of two years. As a first step, the process extracted the non damaging rigid body movement (uniform vertical movement, tilt), then the next step assessed the differential vertical movements through the estimation of the flexural strains. The following conclusions were made:

- The uniform vertical movement is caused by the heave due to frost penetration beneath the sidewalk as the two parameters monitored have the same time dependency.

- During the warm season, the variation of the uniform vertical movements were insignificant as an indication that moisture change doesn't have a significant impact on sidewalks uniform vertical movement.

- Tilt movements were also observed to have the same seasonal dependency as uniform vertical movement. The differential frost heave beneath the sidewalk was explained by the differential soil moisture content at the two edges of the sidewalk.

- It was difficult to understand through this study how the flexural strains vary with seasonal conditions. However, flexural strains were found to be higher during the cold season and a tendency for hogging was observed.

1.3.3   Expansive soil

Expansive soils are classified by the ASTM Soil Classification System, as clays of high plasticity (CH), silts of high plasticity (MH), and organic clays (OH). Table 1.3 shows approximate correlation between plasticity and degree of expansion.

Skempton (1953) defined the activity as being the susceptibility of a clayey soil to expand and suggested three classes of clay. Inactive clay when the activity factor is smaller than 0.75, normal clay for a factor ranged between 0.75 and 1.25; and active clay for a factor greater than 1.25. The activity is defined as follow:

$$Ac = \frac{Plasticity\ index}{Percent\ of\ clay\ particles} \qquad (1.1)$$

Expansive soils can experience large volume changes when the soil swell as it absorbs water or shrinks as it dries. Water content changes in expansive soils occur in the upper few meters under climatic environmental factors. This zone is generally termed as zone of seasonal fluctuation or active zone. Differential movements caused by these volume changes are responsible for severe deteriorations throughout the world (Chen, 1998). Those deteriorations are mostly associated with light surface structures such as pavement or slab-on- grade, while heavy structures tend to eliminate the soil's swelling pressure (Marr et al. 2004).

As mentioned previously, an attempt to find a correlation between the Atterberg limits and the type of sidewalk damage has failed (Rajani and Zhan, 1997). However, the authors

observed that longitudinal cracks increase with plasticity index because a large change in moisture is required to the transition from liquid state to semisolid state. Differential swelling beneath the concrete sidewalk may lead to hogging or sagging, that are responsible for longitudinal cracking.

Furthermore, both freeze-thaw and swelling-shrinkage cycles lead to erosion and void development into the subgrade. Depending on their size, erosion voids may cause a loss of support for the concrete slab. Tensile stresses are then induced and may be critical to the sidewalk integrity.

Table 1.3

Approximate expansion-swell plasticity relationships
(Portland Cement Association, 1983)

Degree of expansion	Percentage of swell	Approximate Plasticity index (PI)
None expansive	2 or less	0 to 10
Moderately expansive	2 to 4	10 to 20
Highly expansive	more than 4	more than 20

Source: This table was taken from the Portland cement association bulletin written by Ralph E. Spears (1983), *Concrete floors on ground: Approximate expansion-swell plasticity relationships*, p.3.

1.3.4   Other causes of deterioration

There are also other causes of sidewalks deterioration. Damage due to the fatigue of the concrete, poor concrete quality or poor concrete construction procedure (placing and curing) are also responsible for sidewalks deterioration. Those causes lead to spalling, pop-outs and scaling.

Trees planted near sidewalks can be problematic to the slab integrity as well. First, the trees may cause moisture depletion during the dry season leading to a tensile-shrinkage mode of failure. Second, some trees have heavy roots that induce pressure that can lift the slab.

1.4   Effect of subsurface void

Investigations regarding the stability of shallow foundations subjected to subsurface voids resulting from mining, tunneling and soluble rock are available and worth noting in this section. The environment of these investigations is different from the scope of the present project as the size of the void and the load applied by the footing are not comparable. Furthermore, those studies don't analyze the behavior of the structure; only soil displacement and the bearing capacity are investigated.

1. 4.1   Influencing parameters

The bearing capacity and the displacement of a strip footing subjected to subsurface void were investigated experimentally and numerically by Baus et al. (1983). The experiments were performed using footings of different widths in a tank holding compacted silty clay where different sizes of void were artificially created. A total of 47 experiments were performed. Numerical modeling was conducted using 2D elastic-perfectly plastic finite element analysis. A normalized critical depth $(D/B)_{cr}$ that represent the limit after which the presence of void has a negligible effect on the bearing capacity of the strip footing was identified. Figure 1.4 shows that the bearing capacity decreased when the voids are closer to the footing (D/B ratio) for a given void size (W/B ratio). This can be explained by the reduction of the shear strength due to the thinner mass of the soil underlying the footing as the void became closer. It can also be observed as illustrated in Figure 1.5 that the critical depth $(D/B)_{cr}$ increased up to a maximum value of 12. This implies that when the depth of the void is located at a distance of more than twelve times the footing width, the bearing

capacity is not influenced by the presence of the void regardless of its size. For the sake of comparison, the critical depth is usually taken as two times the footing width for the case of no void condition.

To determine whether the previous results differ for different void shapes a comparison was made through experimental study (Baus et al., 1983). As shown on Figure 1.6, the void shape has a negligible effect on the bearing capacity as the curves related to the rectangular, square and circular void are very close.

1.4.2   Stability of underground openings

Stability of underground opening have been of interest to many researchers, a centrifuge modeling for instance have been widely used to model stability of soil over cavities. Craig (1990) found through centrifuge tests that failure of clayey soil over a cylindrical void provides a ratio representing the effective overburden depth against cavity diameter of less than the unity. The stability of a cylindrical cavity overlain by a cemented layer of sand was also investigated by Abdulla and Goodings (1996). The authors observed that the failure of the cemented sand layer take either the shape of a truncated conical section or a dome when the cemented layer is 25-30% higher than the cavity diameter.

Analytical approaches to this problem are scarce. Brady & Brown (1993) used analytical approaches based on limit equilibrium to study the stability of a chimney in mining. This method presents some serious limitation. Indeed, the method ignores the plastic flow rules often employing a kinematically inadmissible collapse mechanism and only global equilibrium conditions are satisfied. It is, thus, impossible to determine if a collapse load determined by the limit equilibrium method is safe or unsafe.

Analytical approach based on limit analysis was investigated by Davis et al. (1980). Contrary to the limit equilibrium method, limit analysis is based on the determination of a

safe and an unsafe collapse loads that bracket the true and unknown solution. Therefore, an upper bound solution can be found from a kinematically admissible collapse mechanism by equating the work done by the internal stresses with the work done by the external loads (traction load and self weight of the deforming soil mass). The collapse load determined through this balance will not be lower than the true collapse loads and this is the unsafe solution. The lower bound solution states that if an equilibrium distribution of stress can be found that balances the external loads and is nowhere above the failure criterion of the material, the external loads are not higher than the true collapse loads and this is the safe solution.

Stability of sinkholes and Karst formations are strongly related to arching phenomena. Marston and Anderson theory (1913) stated that the load due to the weight of a soil column supported by a buried pipe is reduced by the arch action that transfers part of the overburden load to the adjacent prism. Therzaghi (1943) used the arching theory to study the stability of soils subjected to underground void. Figure 1.7 represents a soil prism overlying a void assumed to have a width (B). The soil immediately overlying the void behaves in tension (area designated by a) and the overburden load is transferred by cohesive and frictional forces to the adjacent elements. This behavior is known as a true arch (Hunt, 1986) and last momentarily depending on the soil shear strength and other variables. As soil particles begin to drop, the tensile forces that form the true arch start to dissipate leading to a formation of an inverted arch (Figure 1.8). The latter behavior can be described as a soil prism settlement into an inverted arch and mobilize the shear strength of the adjacent soil elements that transfers a portion of the overburden load. The amount of the settlement that forms the inverted arch depends on the distance between the void and the soil element above. As this distance increases, the settlement decreases and ultimately nullifies at a certain point designated by "plane of equal settlement" if the soil thickness is significant.

If a circular void with a radius (r) is substituted to a rectangular void of a width (B), Kezdi (1986) showed that the effect of arching is doubled.

1.5   Underground void detection

A survey involving a detection of voids or void-forming conditions in a residential neighborhood of northern Ohio was conducted by Hauser and Howell in 2001.

A ground penetrating radar (GPR) with a 300 MHz antenna was used in this project to identify locations of roadways that are likely underlain by voids. Figure 1.9 represents a typical cross section of the surveyed roadways reported through boring logs. The sketch shows a layer of asphalt up to 15 cm overlying a 10 cm brick pavement, which overlies 15 cm of concrete.

Initial tests have been made at a location of a known large void to provide a pattern that would be used to track eventual voids elsewhere along the profiles (Figure 1.10). The results obtained revealed a strong amplitude reflection at the base of the concrete pavement in comparison to the usual signal of concrete above soil. Anomalies were also observed in the data related to surface and subsurface facilities such as buried pipes, parked cars, and manhole covers. Each of these anomalies could be identified as such. The authors mentioned that a thinner void would not be observed as distinct, and would separate reflections. However, a combination or interference of the strong reflection at the base of the concrete roadway with the wave of a strong reflection from the bottom of the void can still reveal the presence of a void.

Figure 1.11 shows a map where locations that exhibit the same pattern of the known void are summarized. The signals interpreted as being potential voids were recorded in areas where surface subsidence was observed, such as cracks in roadway pavements, sidewalks, and foundations, as well as pavement patches. This was confirmed by subsequent borings at these areas.
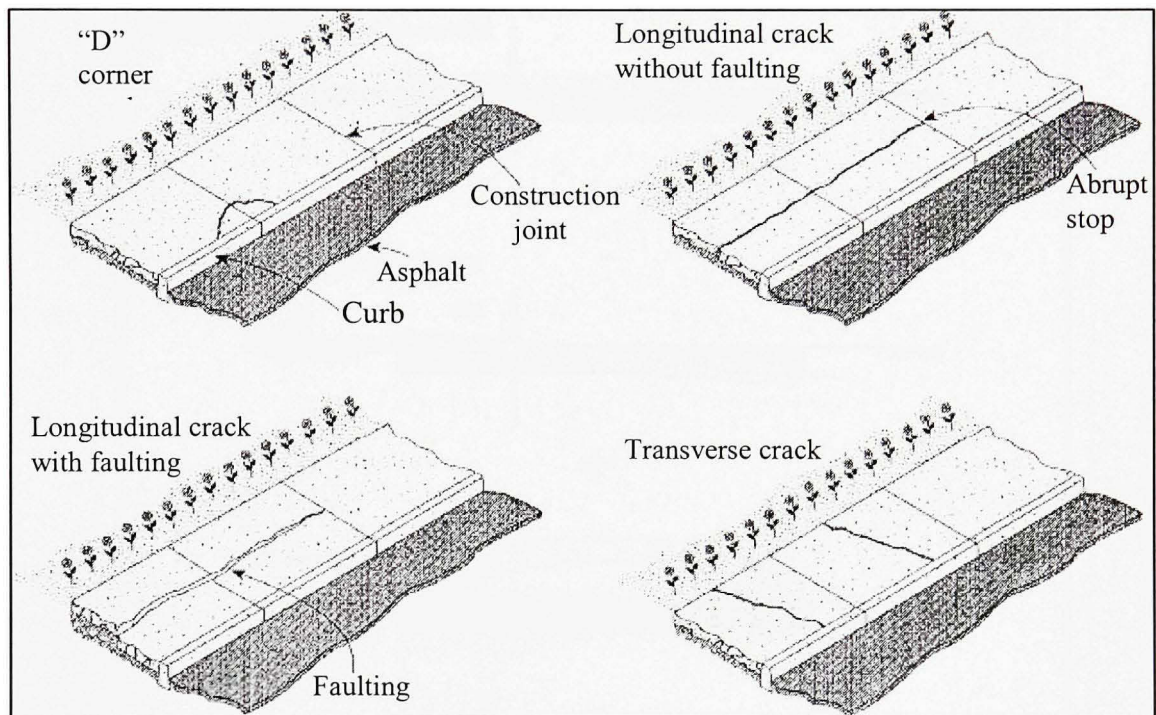
Figure 1.1 *Typical characteristics of sidewalk cracking patterns.*

(Rajani and Zhan, 1997)
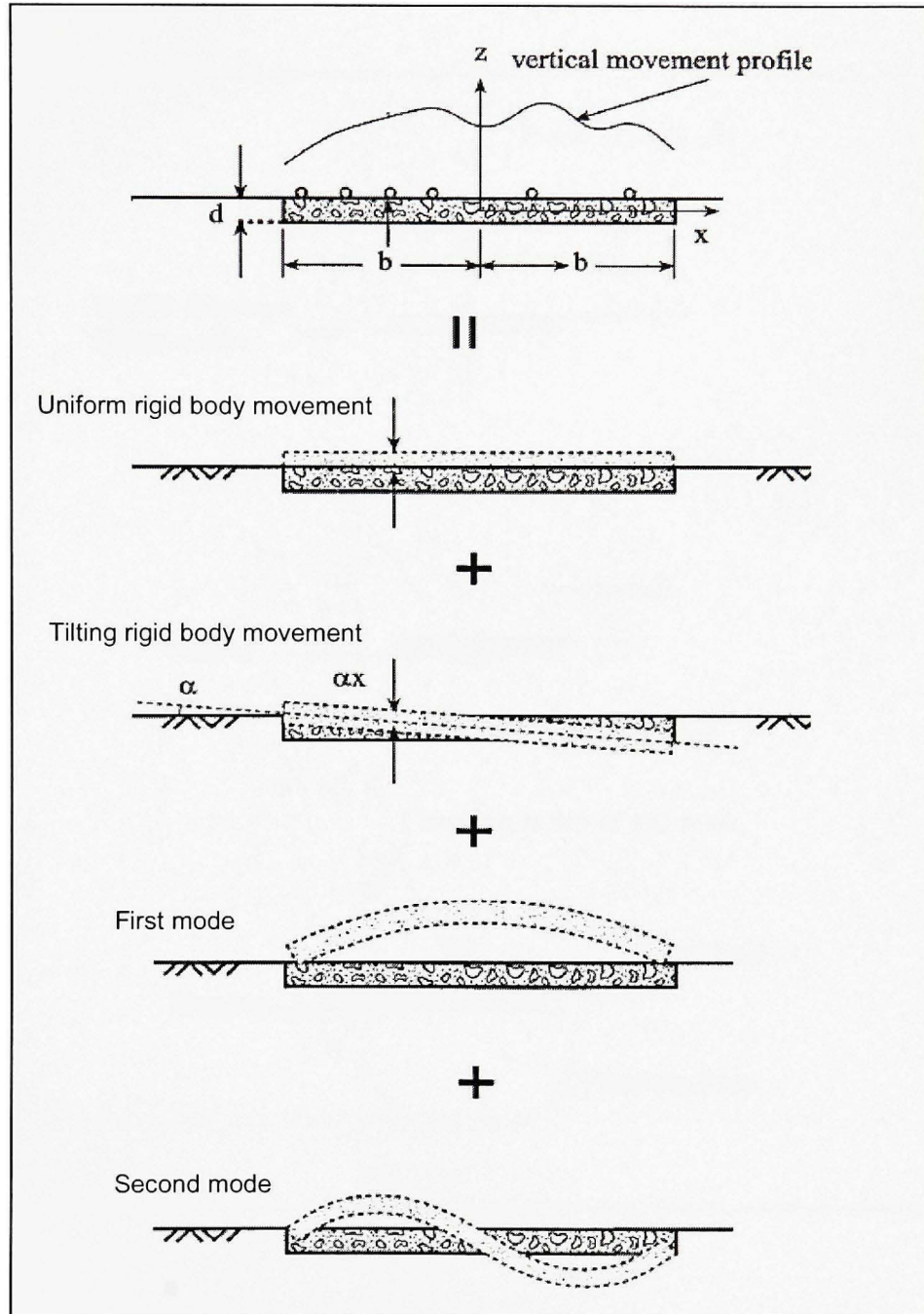
Figure 1.2 *Components of vertical movement for a typical sidewalk slab.*

(Rajani and Zhan, 1997)
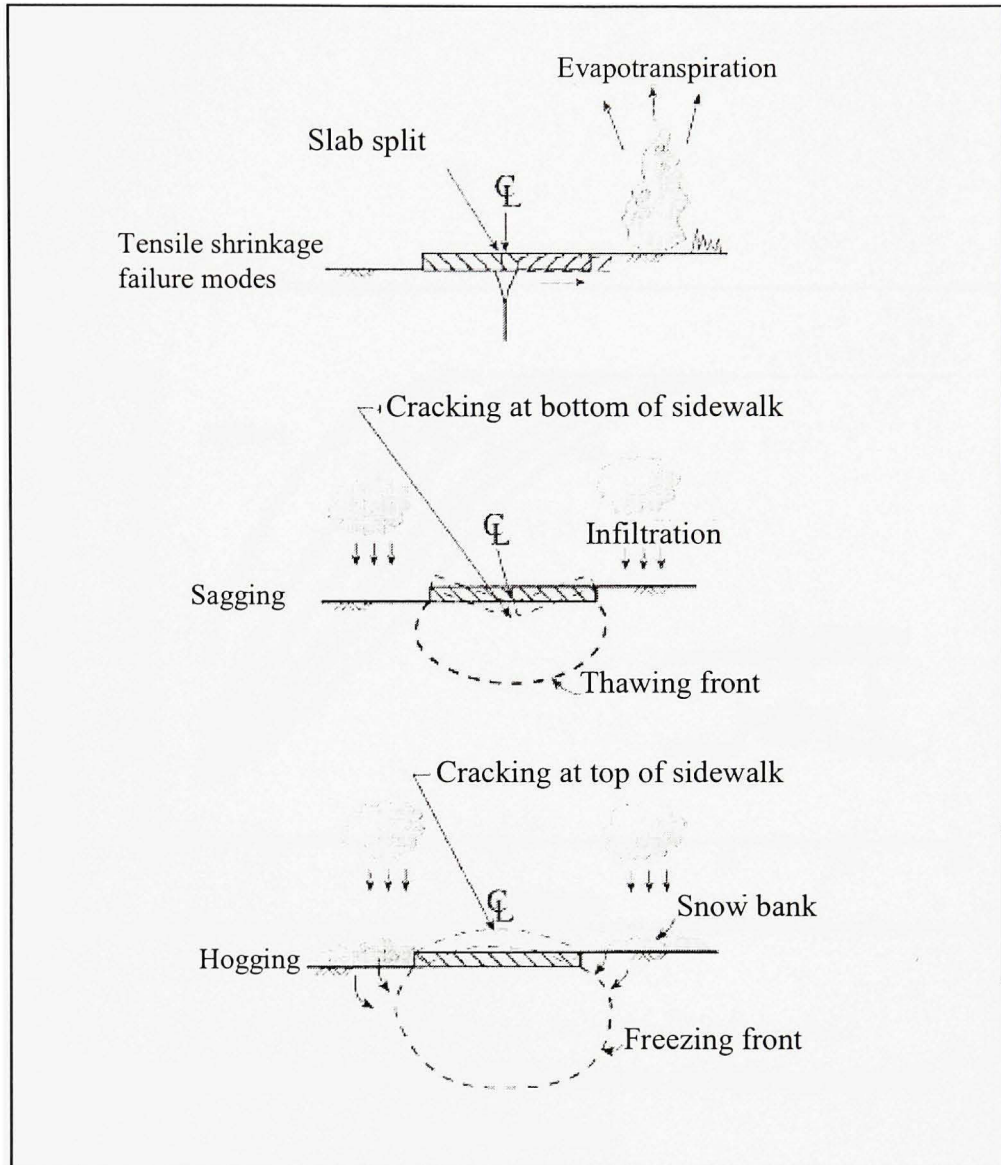
Figure 1.3 *Possible failure modes of sidewalks.*

(Rajani and Zhan, 1997)
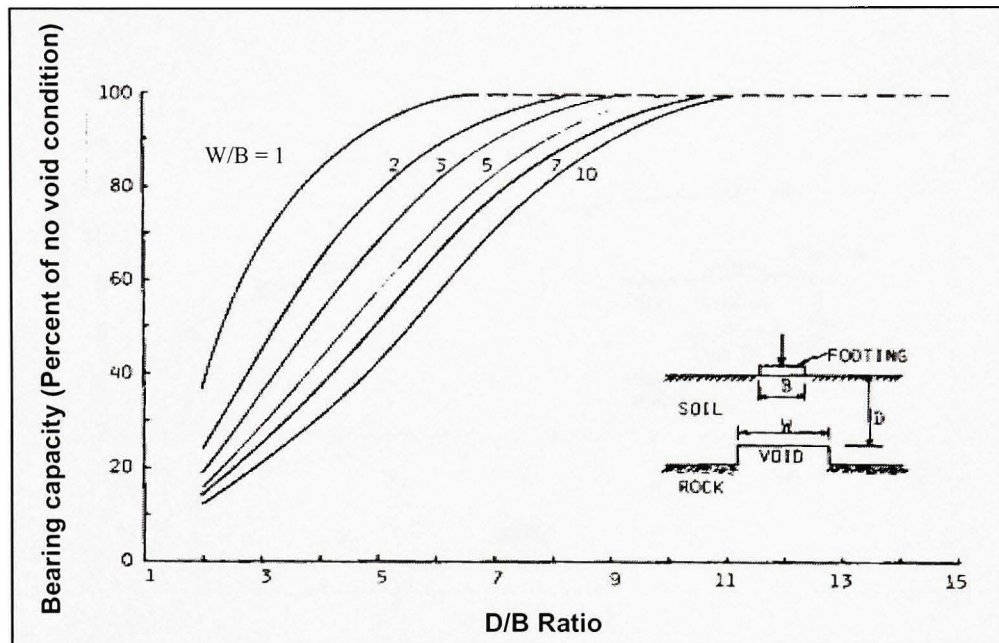
Figure 1.4 *Effect of void size and location on the bearing capacity*

*of a strip footing.*

(Baus et al. 1983)

Figure 1.5 *Effect of void size on critical depth to void.*

(Baus et al. 1983)

Source: This figure was taken from an article written by Ronald L. Baus (1983), *Bearing Capacity above void: Effect of void size on critical depth to void*, p.10 . Published by the Journal of Geotechnical Engineering v 109, n 1, pp. 1-14.
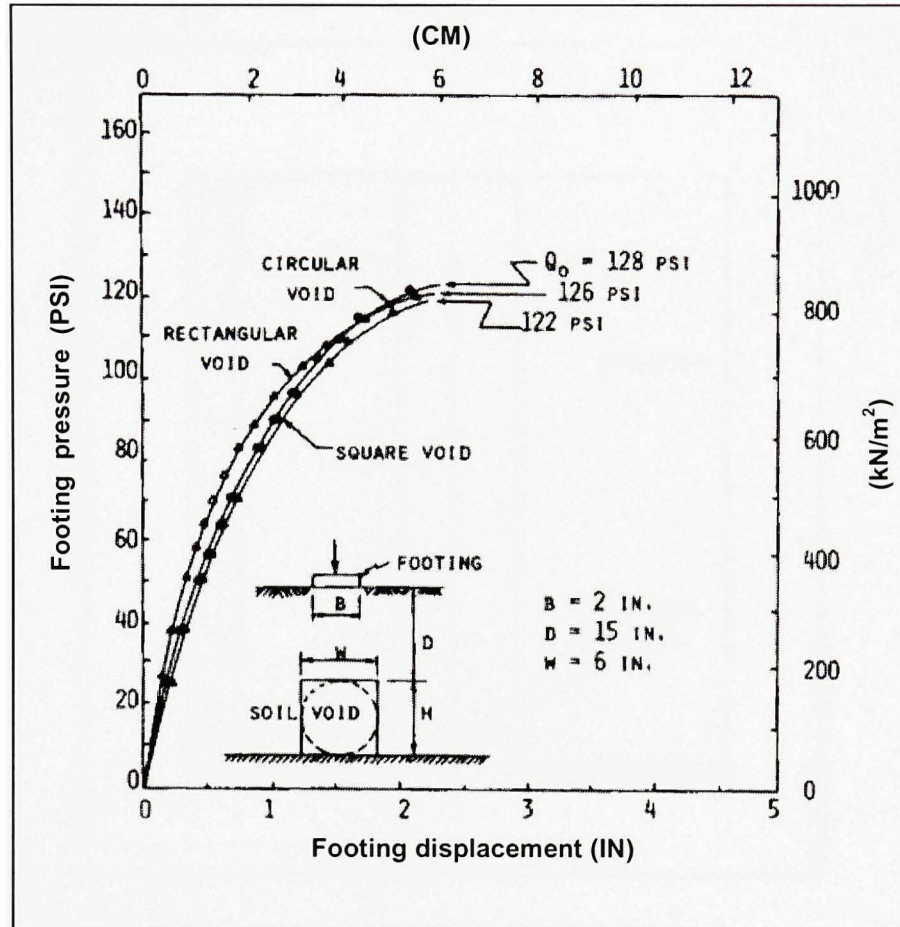
Figure 1.6 *Effect of void shape on bearing capacity of strip footing.*

(Baus et al.1983)
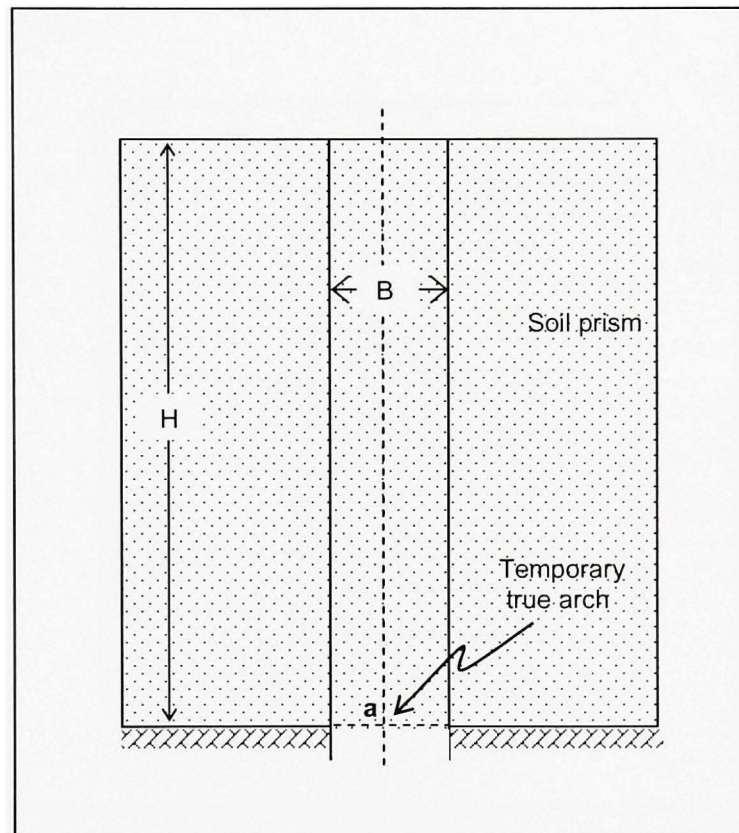
Figure 1.7 *True arch behavior.*

(McKelvey III, 1994)

Source: This figure was taken from an article written by James A. McKelvey III (1994), *The anatomy of soil arching: Void develops beneath soil mass*, p.321. Published by Geotextiles and Geomembranes v 13, n 5, pp. 317-329.
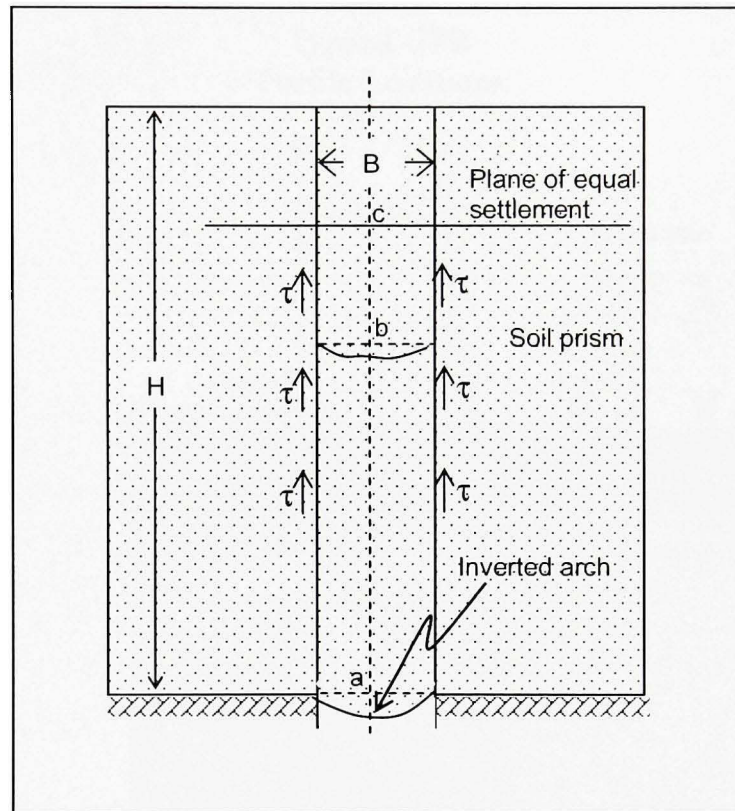
Figure 1.8 *Inverted arch behavior.*

(McKelvey III, 1994)
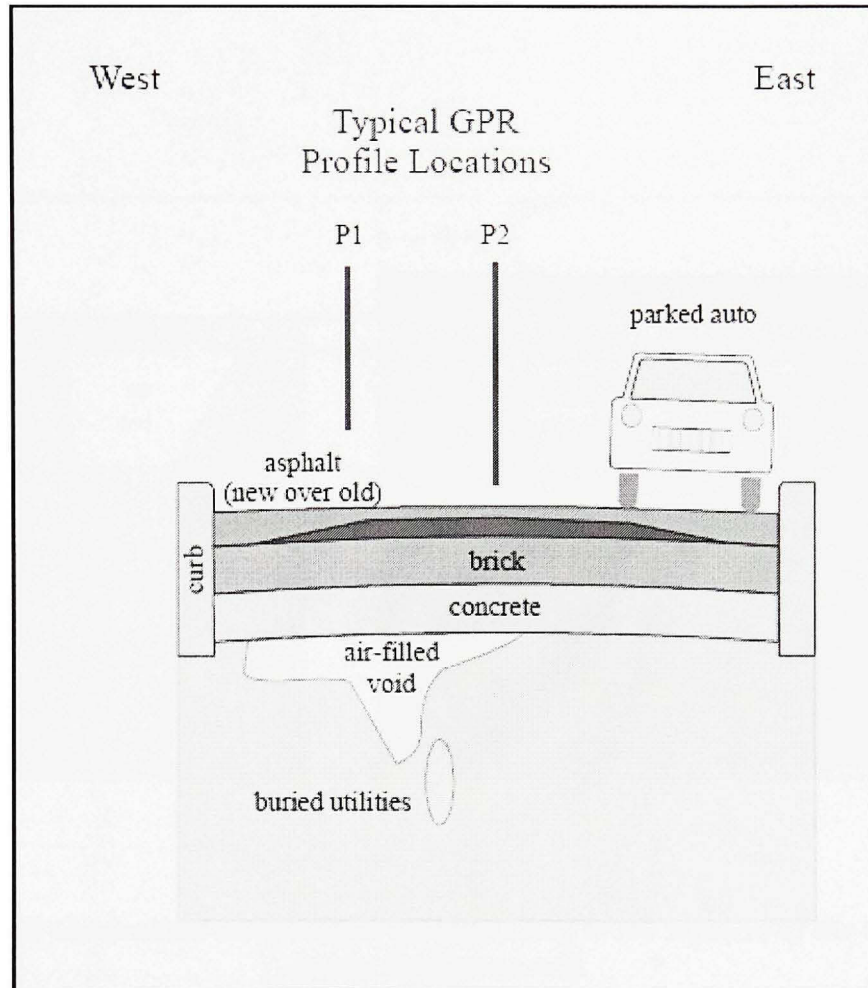
Figure 1.9 *Generalized cross section of the roadways profile.*

(Hauser and Howell, 2001)

Source: This figure was taken from an article written by Ernest C. Hauser and Mark J. Howell (2001), *Ground penetration radar survey to evaluate roadway collapse in northern Ohio: Generalized cross section of the roadways profiled and the location of the main GPR profiles within the roadway,* p.3. Symposium on application of geophysics to environmental and engineering problems, 7 p.
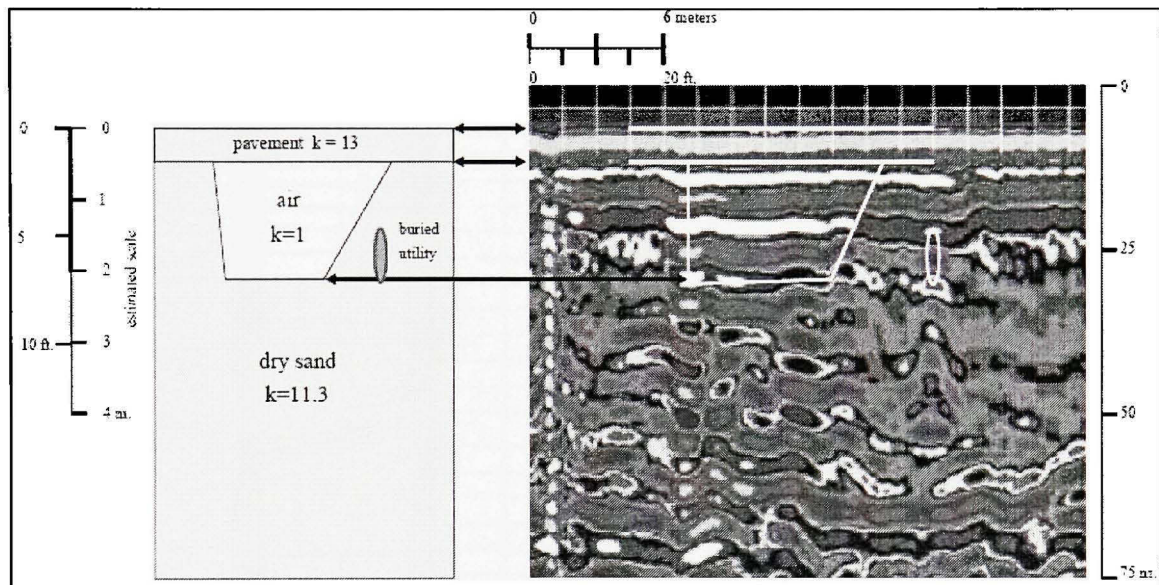
Figure 1.10 *Generalized cross section corresponding to the segment of the GPR data across the known void.*
(Hauser and Howell, 2001)

Source: This figure was taken from an article written by Ernest C. Hauser and Mark J. Howell (2001),
          Ground penetration radar survey to evaluate roadway collapse in northern Ohio: Generalized
          cross section of the roadways profiled and the location of the main GPR profiles within the
          roadway, p.6. Symposium on application of geophysics to environmental and engineering
          problems, 7 p.
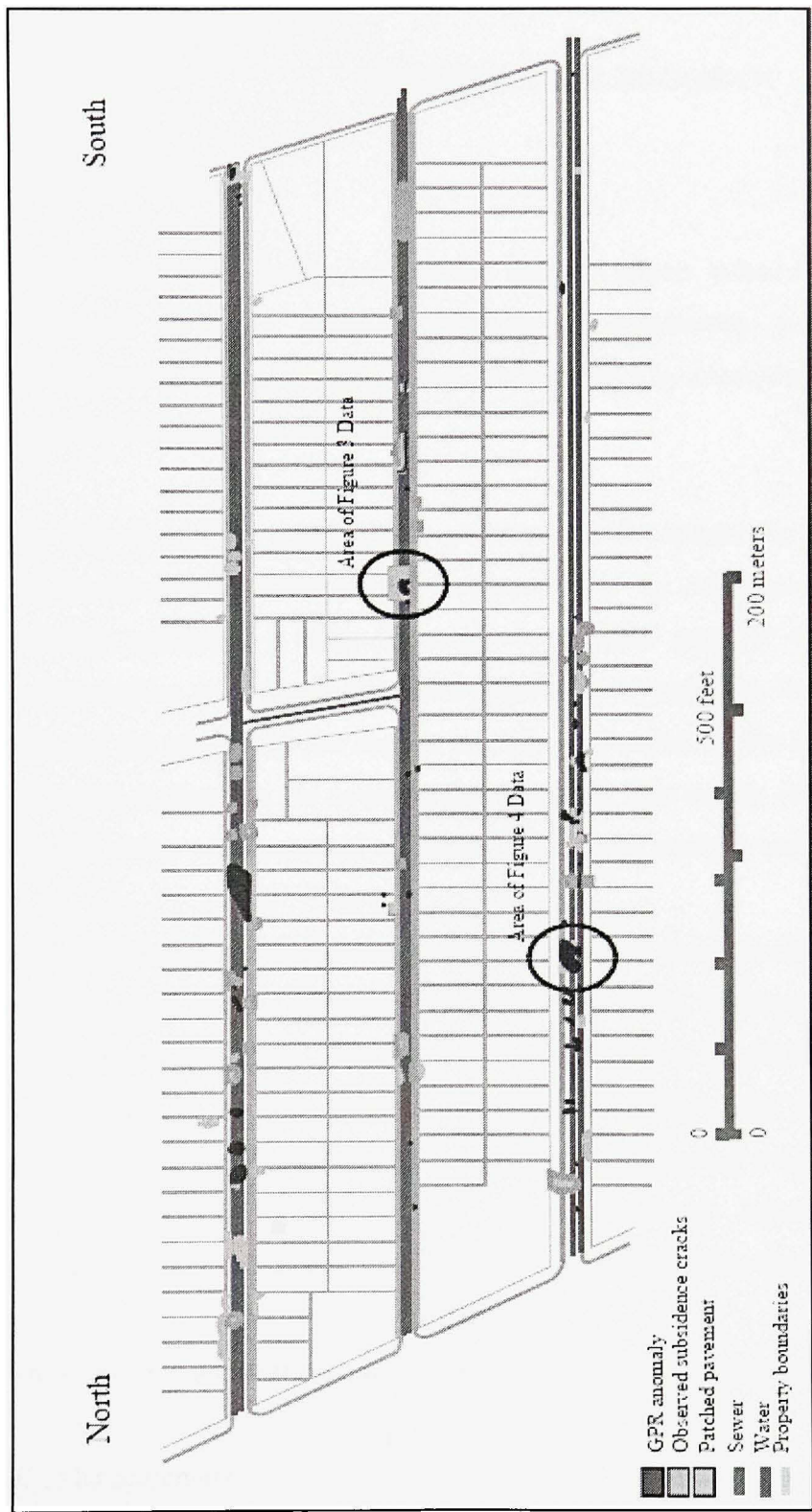
Figure 1.11 *Map of the streets profiled showing the distribution of GPR signals.*

(Hauser and Howell, 2001)

Source: This figure was taken from an article written by Ernest C. Hauser and Mark J. Howell (2001), *Ground penetration radar survey to evaluate roadway collapse in northern Ohio: Map of the streets profiled in this study showing the distribution of GPR anomalies suggestive of voids and the distribution of subsidence features and patched pavement,* p.7. Symposium on application of geophysics to environmental and engineering problems, 7 p.

CHAPTER 2

EXPERIMENTAL PROGRAM

2.1   General

The process of subsurface soil erosion and the effects induced on the ground surface is considered to be a complex geotechnical engineering problem and experimental investigations are limited. The design methods used by consulting engineers rely mainly on empirical or numerical analysis.

The objective of the experimental program is to investigate the performance of a slab-on-grade subjected to subsurface soil erosion. One of the challenges is to develop a method to simulate artificially a three dimensional void into granular materials and measure the corresponding ground response. Two cases were investigated, the case where the surface is free and the case where the surface is uniformly loaded. As for the latter, a rigid steel plate was used to simulate the concrete slab-on-grade. The results of this investigation allowed the calibration of a numerical model and running the analysis under full scale conditions.

In developing this experimental program, techniques that have been successful in tunneling research were tested (Terzaghi, 1936; Terzaghi, 1943; Atkinson et al., 1975; Higawara et al., 1999; Sharma et al., 2001; Wu et Lee, 2003; Lee et al., 2006). However, some of them were found to be not accurate enough (repeatability and precision) to be taken in consideration. Finally, the physical model built consisted of a rigid steel tank to contain the sand, a mechanism to simulate one dimensional subsurface soil erosion and instrumentations to measure the ground response either when the surface is free or loaded.

The relevant parameters that need to be measured at the ground surface are listed as follow:

a. The settlement.
b. The strain.

c. The surface contact pressure between the ground surface and the loading element.

d. The effect of the void shape

The roadmap of this chapter is as follows. Section 2.2 will describe the steel tank built to contain the sand and all attempts used to simulate the formation of subsurface void. Those that were not successful will be described as well to explain the process that led to the final setup. Section 2.3, 2.4 and 2.5 describe the instrumentation, the specification of the materials used and the experimental procedure, respectively. Finally, results of the experimental investigation will be discussed in section 2.6.

2.2   The physical model

The physical model is composed of a rigid steel tank to hold the sand, a mechanism to simulate artificially subsurface soil erosion and a rigid steel plate for the loaded tests. The latter is described in the section 2.4, dedicated to the material properties. Some hypotheses have been made during the development of the experimental program:

a. The set up built represents a 2D problem (plane strain).

b. The possible effects of the lateral boundaries were neglected.

c. An ideal soil (silica dry sand) was used during the experiments.

2.2.1   The rigid box

Figure 2.1 shows the (1^Hm×1.46^Lm×0.3^Wm) rigid rectangular tank built to hold the sand. The tank was made using 6 mm thick steel plates joined with 6 mm steel bolts. The rigidity of the tank is an important parameter since any deformation of the latter will influence the measurements that will be taken. To improve the rigidity, both the front and rear sides were reinforced with three 100 mm HSS sections. The front side had to be made of a colorless material to allow visual observations; a 6 mm Plexiglas sheet was then used. The internal

sides of the tank were painted and lined with plastic sheets to reduce friction between the sand and the sides of the tank.

To simulate the unloading process due to subsurface void, the following techniques were investigated:

- Polystyrene foam and organic solvent
- Pressurized air bag
- The trap door

Several experimental challenges were encountered when the first two methods were adopted; in particular problems related to test repeatability. For the sake of complement these methods are described in the following sections.

2.2.2   Polystyrene foam and organic solvent

This method was developed by Sharma and al. (2001) to simulate unloading due to excavation during a tunneling process. The technique is very straightforward. When polystyrene foam is exposed to an organic solvent it dissolves very quickly. This technique was adapted to our experiment by burying a half sphere of polystyrene into a tank full of sand. Acetylene was the dissolving agent used in this experiment. When the acetylene is injected and gets in contact with the polystyrene it dissolves leaving a half-spherical void in the soil (Figure 2.2). However, to avoid the mixing of the surrounding sand with the acetylene, the polystyrene was sealed with an impervious plastic wrap. Two hoses were also connected to the bag to introduce the acetylene and evacuate the gas generated by the chemical reaction (acetylene + polystyrene). The idea was abandoned after several trials for the following reasons:

a. The exact amount of acetylene was hard to introduce because of the chemical reaction between the acetylene and the polystyrene into the plastic wrap. This has led to a non complete dissolution of the polystyrene foam and a preferential movement of the sand.

b. Due to the pressure needed to introduce the acetylene, leakage from the plastic wrap was observed and could not be avoided. This may have changed the characteristics of the sand by the acetylene.

Following the same concept another combination (i.e. wax+ heat) was tested and showed little success because of the non uniform melting of the wax inside the void.

2.2.3   Pressurized air bag

Several researchers have used pressurized air bag to simulate subsurface voids in tunneling (e.g. Atkinson and al., 1975; Higawara and al., 1999; Wu and Lee, 2003; Lee and al., 2006). However, the first objective of this research had to be modified from a three dimensional to a two dimensional subsurface void shape. Figure 2.3 shows the different elements of the test setup. A rubber bag is inserted into a cylindrical steel net and buried into the sand. At the initial stress state, the bag is pressurized to fit the shape imposed by the cylinder and reach the overburden pressure. Unloading mechanism is then simulated by lowering the air pressure, allowing the movement of the sand particles into the cylinder through its nets. As shown in Figure 2.3, the air pressure is injected by a compressor through a hose, and controlled with a pressure gage. Two different rubber bag materials were used: stretchable commercial balloons and non-stretchable lined geotextile used in commercial shipping (Dunnage bags) sealed with a heat gun. Experiments were not successful because of the air leakage due to the amount of air pressure that had to be induced into the bag.

2.2.4   The trap door

The trap door technique was first developed by Terzaghi (1936, 1943) to explain the arching theory. This technique was adopted to simulate a one dimensional soil loss below surface. The trap door consisted of two sliding plates whose movement can easily be controlled by a threaded bolt and nut mechanism. These sliding plates cover a rectangular opening at the base of the tank as shown in Figure 2.4. After several trials, a 5 mm opening was found to provide sufficient control over the sand movement. A collector container is placed under the opening to control the sand loss. When the collector container is full, no more sand is allowed to move out from the trap door and the test is considered complete. A total volume of 2670 cm^3 of sand was removed from the bottom of the box in each test.

For the sake of convenience the vertical movement of the collector container that controls the sand volume loss was managed using a hydraulic jack.

2.3   Instrumentation

Measuring the soil response to subsurface volume loss has always been a challenge because of the cohesionless nature of the sand. As mentioned previously several parameters were planned to be measured at the surface but only some of them were found to be accurate enough to be taken in consideration. All the monitoring techniques investigated are described below.

2.3.1   Measuring the displacement

Two optical displacement transducers were used to measure the displacement of the sand surface when unloaded (free surface). Two measurements were taken, one at the center line and the other at 150 mm from the center line. The transducers (BANNER LG5A65NIQ) can measure a displacement up to 150 mm. The results of the sensor calibration are plotted on Figure 2.5. It can be seen that the correlation between the voltage generated by the

transducer and the displacement measured are quite linear. The transducers are connected to the data acquisition unit and an external power supply to provide 15 V excitation. Each transducer is fixed to a steel bracket and screwed to an aluminum bar that can be lowered to within a certain distance above the sand surface. Since the laser generated by the optical transducers is reflected only on a dark surface, a small amount of sand was painted in black right where the laser aims. Figure 2.6 shows the details of the two optical displacement transducers and their installation at the top of the tank.

In addition to the displacement recorded using the optical transducers, manual measurements of the final width and depth surface profile were also taken.

2.3.2   Measuring the contact pressure

The redistribution of the contact pressure (vertical stress along the contact surface between the plate and the sand) is measured using load cells (SCAIM-AL5KG). The load cell has a strain gage glued all along its top surface and works as a cantilever. One end is fixed to the plate and the other is free to move through a hole made into the steel plate. The differential movement of the cell when the sand is removed from the tank induces a deformation to the strain gage and is converted to an equivalent load on the cell. An aluminum disk is screwed to the free end of the cell to increase the sand contact area. Two load cells have been placed at two chosen locations in order to allow for continuous contact with the sand surface during the duration of the test (Figure 2.7). A calibration needs however to be conducted since the cell measures loading and not pressure. A waterproof parallelepiped made of wood was built, whose base was constituted of the steel plate provided with the load cell. The whole device was immersed in a water reservoir at different depths (Figure 2.8). The loads measured by the cell at each depth were calibrated with the hydrostatic pressure (ρgh). Where ρ, g and h are the density of the water, the gravity and the water elevation, respectively. The results of the calibration are plotted in Figure 2.9.

2.3.3   The data acquisition system

The signals recorded by the optical displacement transducers and the load cell were transmitted to an IOtech (Strain Book /616) data acquisition unit, connected to a Compaq Presario SR2170NX desktop computer (Figure 2.10).

2.4   Material properties

a) The sand

The experiments were conducted using an ideal soil (silica dry sand) commercialized by *Quartz Industrial* under the designation 2075. Results of the sieve analysis (Figure 2.11) according to the USCS standard indicated that the sand particles were coarse with little or no fines.

b) The steel plate

For the loaded tests, a steel plate was used to simulate a rigid slab-on-grade. Consequently, two 50 mm HSS sections were welded all along the length of the plate to increase its rigidity. The length, width and thickness of the steel plate are 1.4 m, 0.3 m, 6×10^{-3} m respectively (Figure 2.12). The specifications based on the ASTM are summarized in Table 2.1.

Table 2.1

Steel plate specification
(ASTM-A36)

Tensile strength (MPa)	Yield (MPa)	Young modulus (E) (MPa)	Poisson ratio (υ)	Weight (kg)
400-550	250	2×10^5	0.3	44.54

Source: Material property data, *ASTM A36 Steel plate: Mechanical properties*,
           < http://www.matweb.com >, consulted on December 2007.

2.5   Experimental procedure

In order to have the same sand density for each test, an experimental procedure was developed to fill the tank with sand. A plastic container (81.3 cm × 51.4 cm × 42.2 cm) was used to fill the tank in several layers of 0,175 m in thickness. First, the plastic container is filled from a reservoir where the sand is stored and placed at the top of the tank using a fork lift. Then the sand is poured from the container into the tank, and manually graded into a uniform layer. No compaction was applied and the same sequences were repeated for each test to minimize potential inconsistencies. The placement procedure is repeated until the sand surface reaches the desired height. Each test defined by its height required a sand volume that corresponded to a number of containers as shown in Table 2.2.

Figure 2.13 shows a cart provided with three wheels that can be slid back and forth along two rails welded at the top of the tank. An aluminum plate fixed vertically to the cart grades the surface of the sand. This device was used to grad the last layer of sand as it needed to be perfectly flat, in order to optimize the accuracy of the measures taken at the surface.

Once the tank is prepared into uniform layers, 2670 cm^3 of sand are removed from the tank through the trap door. The above procedure is illustrated using a picture taken for each step in Appendix IV.

Two series of tests were conducted during the experimental program. The first series is conducted under unloading conditions (free surface) and composed of five tests of different heights (0.175 m, 0.34 m, 0.5 m, 0.64 m, 0.8 m). In this first phase, the movement of the surface profile was measured with the optical transducers and the final profile of the deflection was taken manually. For the loaded tests only one height (H = 0.8 m) has been chosen. This second series of tests was conducted under the same conditions; however a uniform load was applied at the surface by a rigid steel plate. The contact pressure was monitored at two specific points with a load cell and the final profile of the deflection was reported as well.

Table 2.2

Sand surface heights vs Number of containers

Sand surface heights (H) (m)	Number of containers
0,175	1
0,34	2
0,5	3
0,64	4
0,8	5

2.6   Results analysis

Two parameters were found accurate enough to be taken in consideration through the experimental program: The contact pressure and the displacements at the surface. Each parameter and its results will be discussed in a dedicated section.

2.6.1   The surface displacements

In order to understand the displacements generated by the subsurface sand volume loss, vertical displacements located at the center line and at 0.15 m from the center line are plotted in Figures 2.14 and 2.15 respectively for several heights. Both figures represent the settlement versus time for the case of a free sand surface. It appears that the curves that decrease after reaching a certain value, can be explained by the fact that the displacement experienced at this location is higher than the optical transducers are able to measure (out of range). Thus, since the final displacement can not be measured with the optical transducers, they were reported manually and are displayed on each curve on Figures 2.14 and 2.15. Figure 2.16, illustrates the surface settlement profile corresponding to each height for the case of a free sand surface. The settlement is characterized by its width B and the depth D at the center line.

Based on Figures 2.14 and 2.16 it can be concluded that the height H is proportional to the width B and inversely proportional to the settlement. Indeed, as the height is increased, the settlement decreases while the width B increases. This mechanism can be explained by the slope of the curves in Figure 2.14 that represents the rate of particle movement through the trap door at the bottom of the tank and the upward propagation to the surface. As the height increases, more time is needed for this movement to reach the surface at the center line, and more time is needed for the rearrangement of the sand particles, resulting in a larger width B and a smaller depth D.

For the loaded tests represented by Figure 2.17, the settlement at the centre line was found to be the same compared to the one of a free surface (12 mm) while the width B is larger (0.58 m) for the loaded surface as compared to 0.46 m for a free surface.

2.6.2   The contact pressure (vertical stress at the surface)

Four tests were conducted to measure the contact pressure of a loaded surface. To ensure the repeatability of the experiment, the tests were performed using the same sand height (H=0.8 m). Three measurements were recorded at a horizontal distance of X=1.23 m and one at the symmetrical opposite side (X=0.23 m). As shown in Figure 2.18, it was observed that before the unloading process (sand removal) is initiated, the initial contact pressure was different for the four tests. This was corrected by offsetting the reading to a consistent value that represents the expected pressure due to the weight of the plate (1.01 kPa). Figure 2.19 shows the variation of the contact pressures initiated from the same point that corresponds to the initial contact pressure, estimated as the ratio between the weight of the plate and its contact area. It can be seen that during unloading the contact pressure increases up to a certain peak of 1.26 kPa, 1.22 kPa, 1.21 kPa and 1.16 kPa for the four tests respectively.

The significance of these results is that the unloading process forces the sand particles supporting the plate, to redistribute along the latter from the central line to the sides, where the sand surface and the plate are still in contact. This redistribution allows the rearrangement of the sand particles and arching will develop in the soil. Indeed, arch action allows a new equilibrium to be established by transferring the load induced by the plate to the adjacent soil prism. This process would continue if the unloading process was not stopped, until the eventual failure of the soil prism. In some cases, the pressure drops after the peak because the sand particles have moved around and rearranged such that the pressure reaches a more uniform distribution.

100 mm HSS section

Front side: 6 mm Plexiglas

100 mm HSS section

1.46 m

100 mm HSS section

1 m
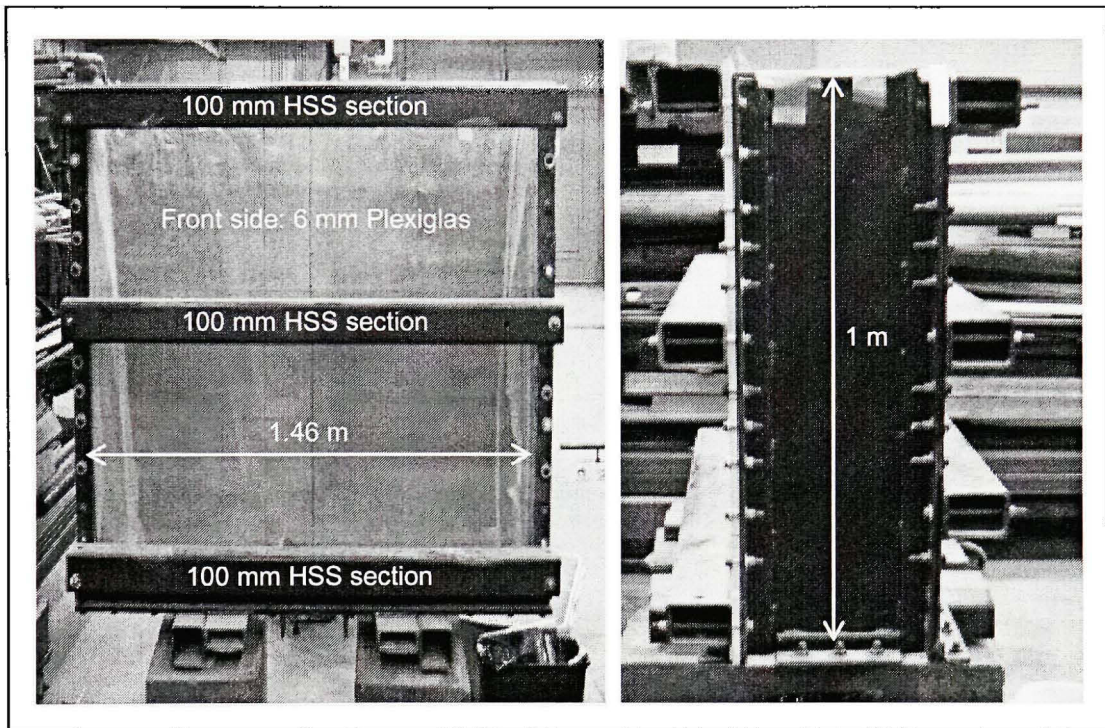
Figure 2.1 *Description of the rigid steel tank.*
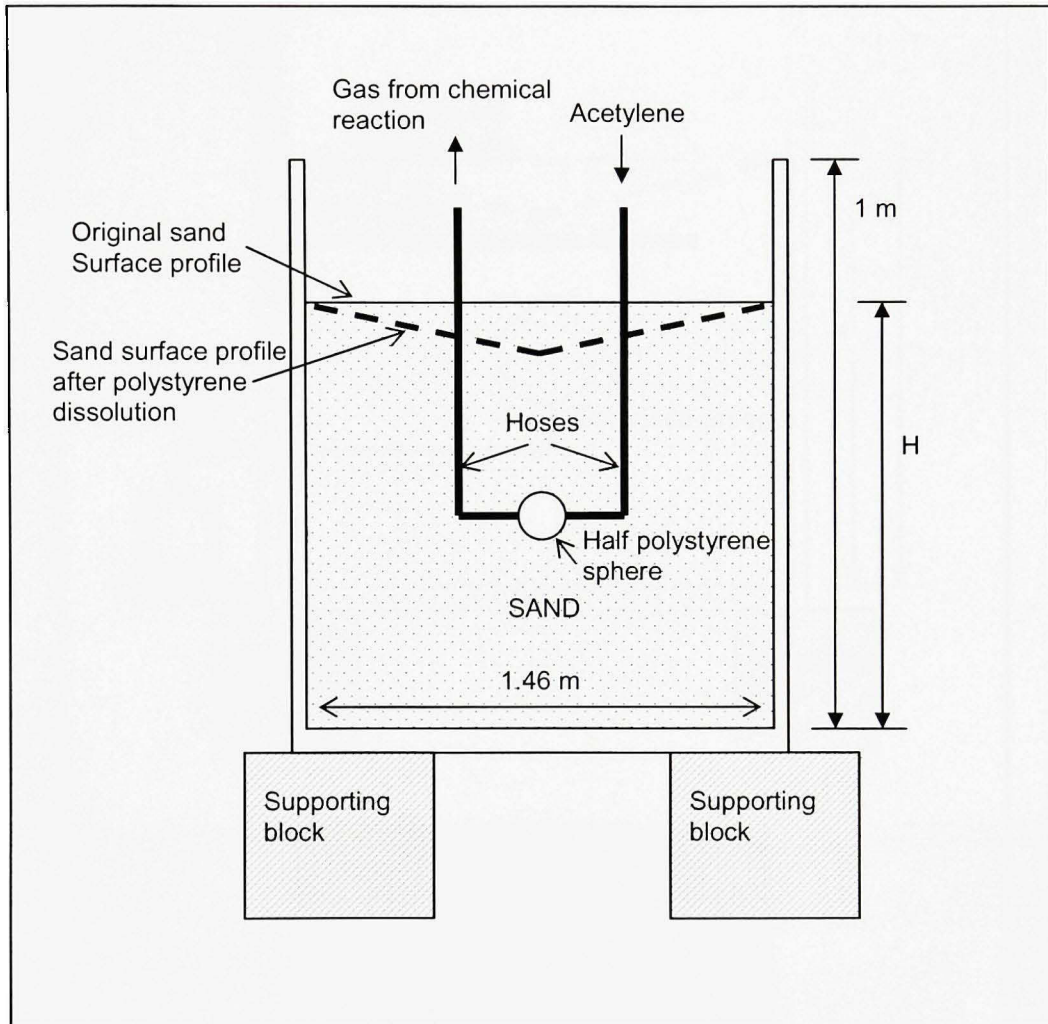
**Figure 2.2** *Polystyrene foam and organic solvent technique.*
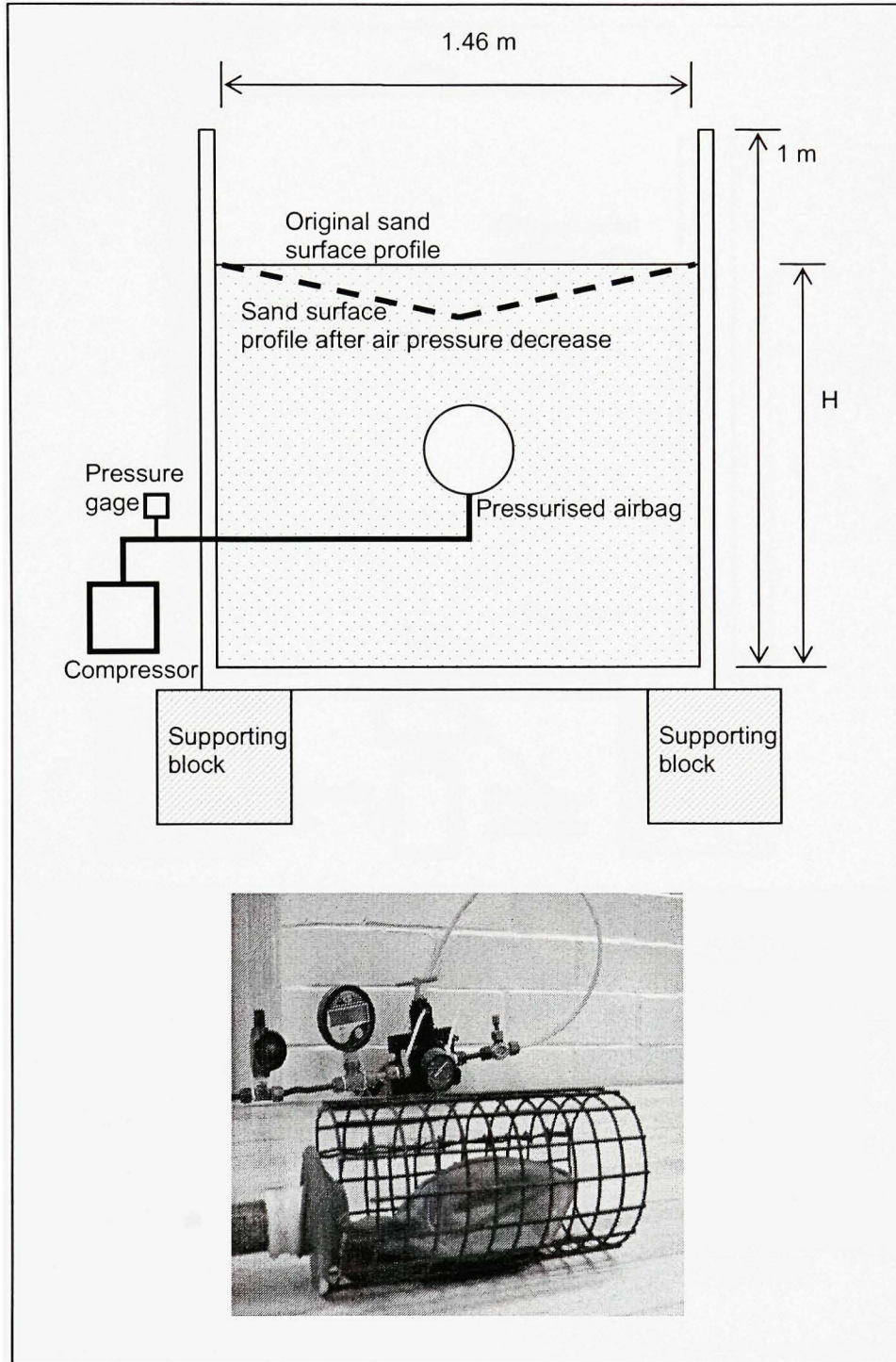
**Figure 2.3** *The pressurized airbag technique.*
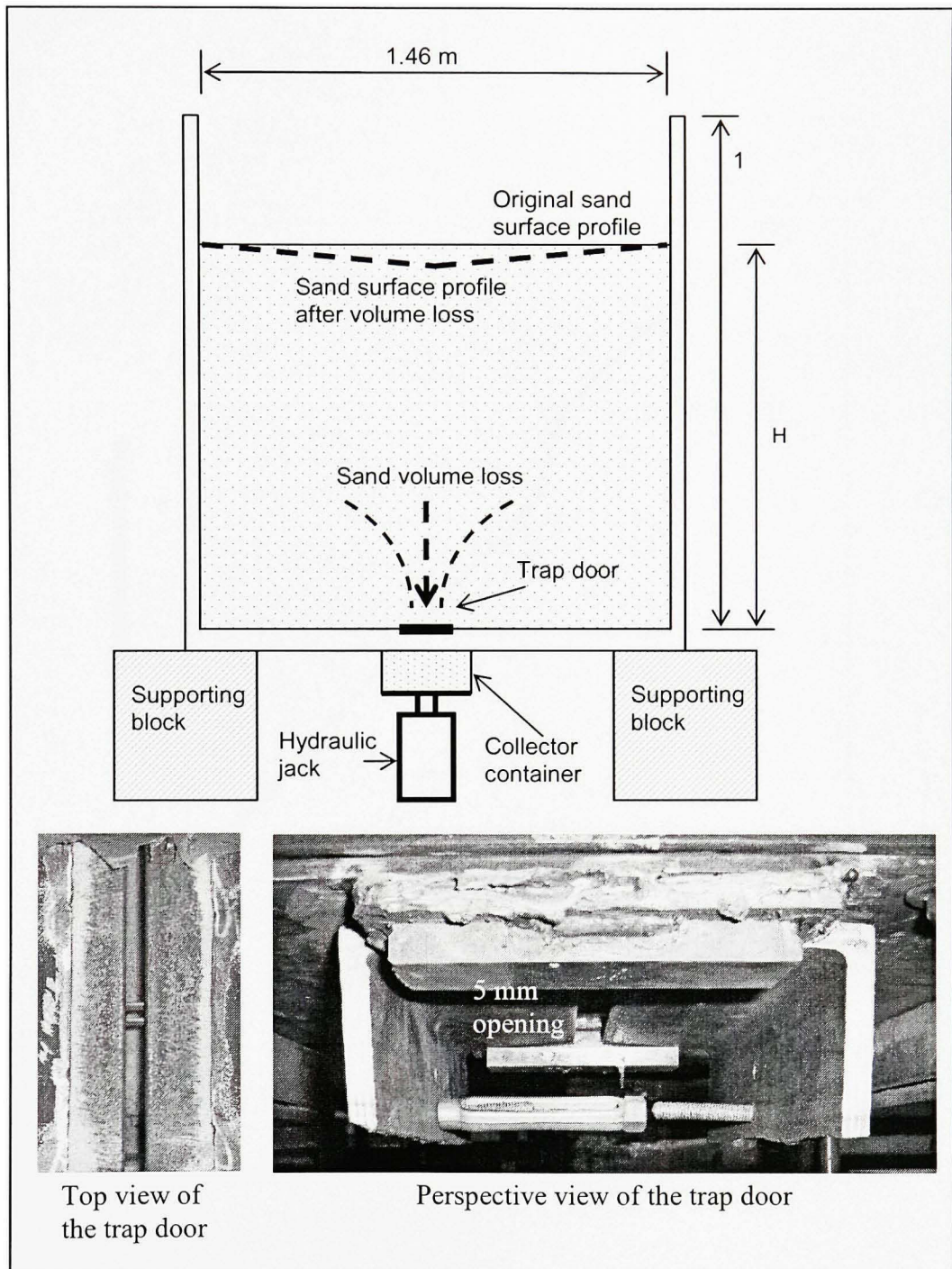
Figure 2.4 *The trap door technique.*
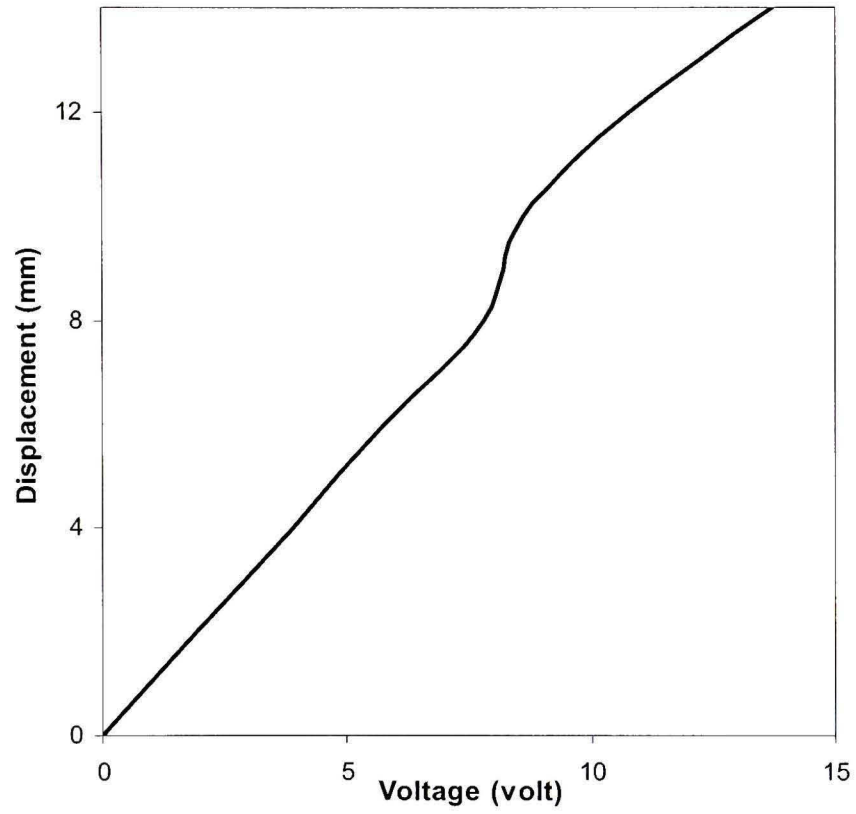
**Figure 2.5** *Result of the optical displacement transducers calibration.*

48
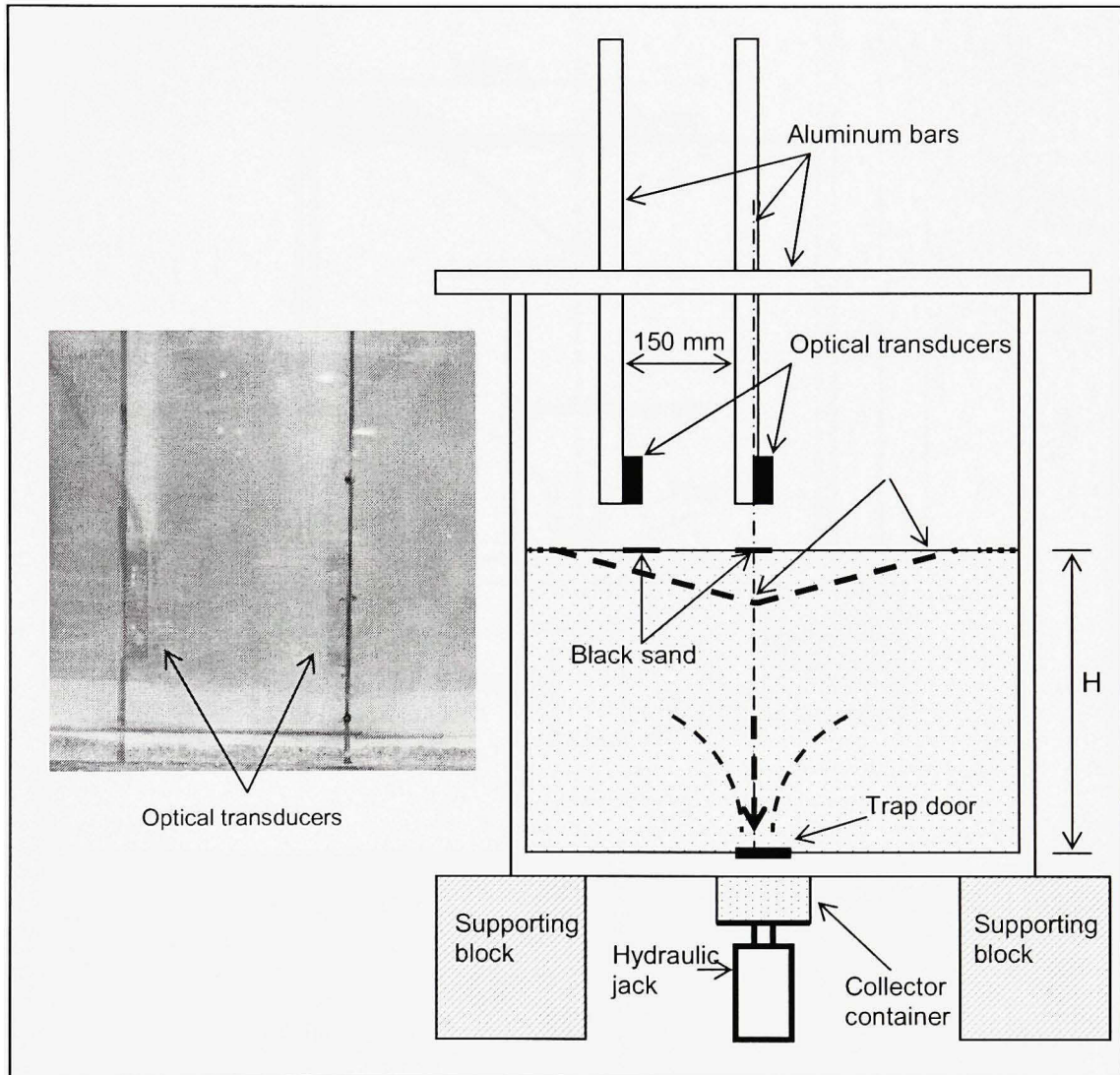
**Figure 2.6** *Displacement set up.*
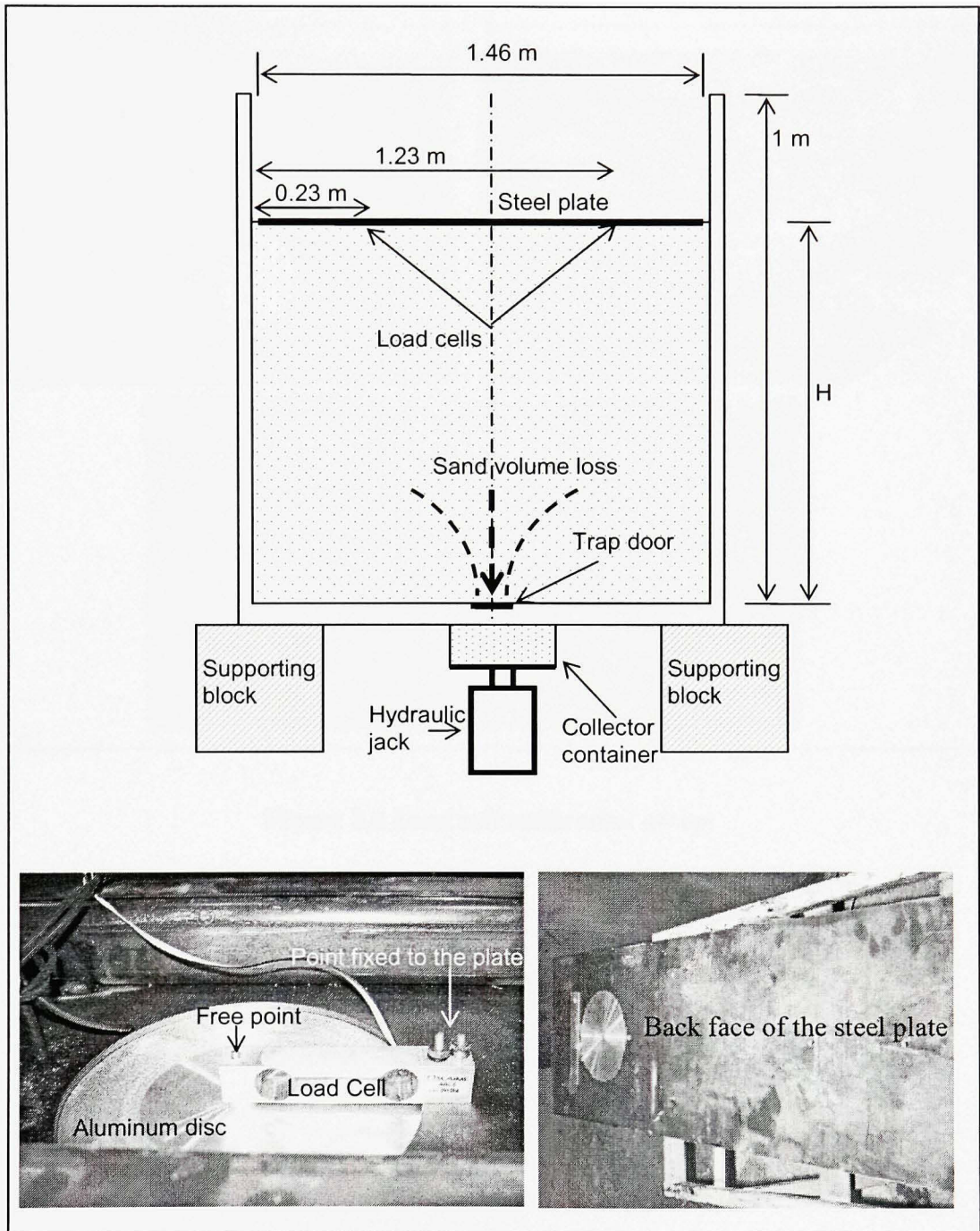
Figure 2.7 *Contact Pressure measurement set up.*
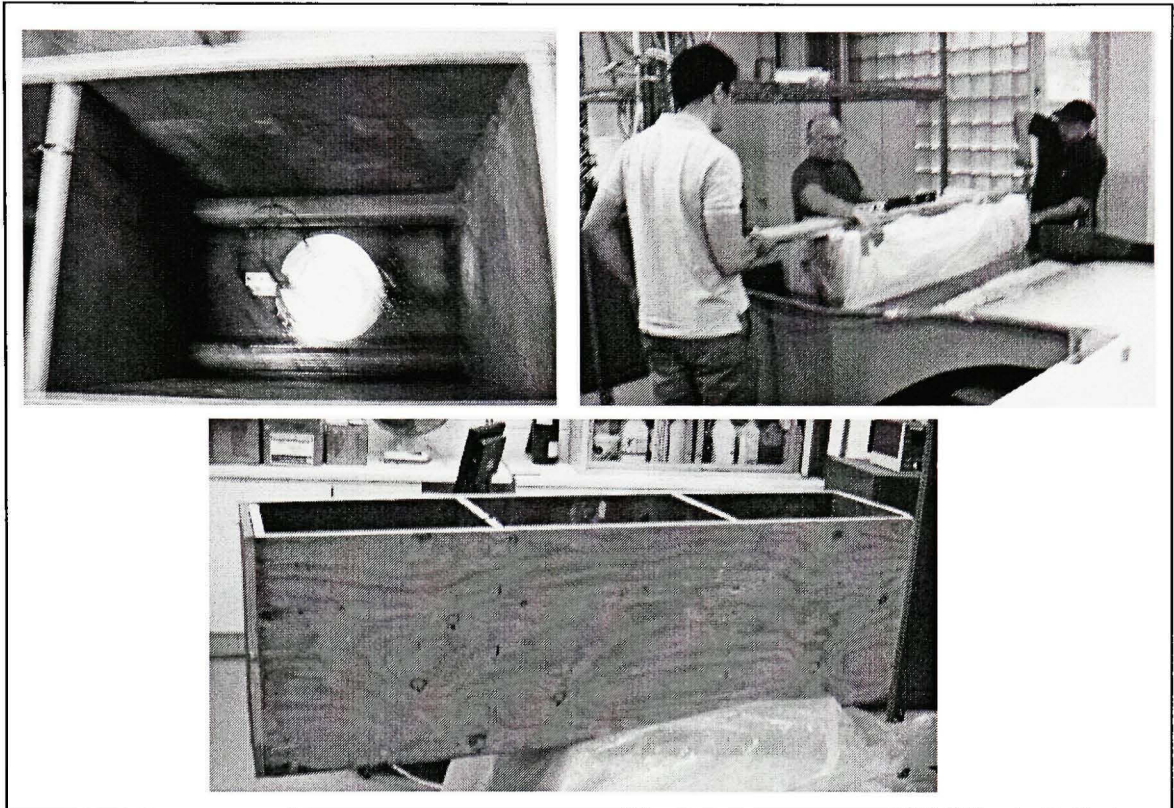
Figure 2.8 *Load cell calibration set up.*
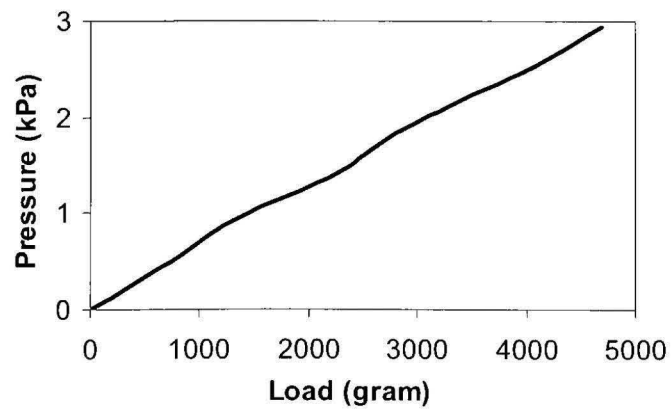
Figure 2.9 *Result of the load cell calibration.*

Figure 2.10 *The data acquisition system.*
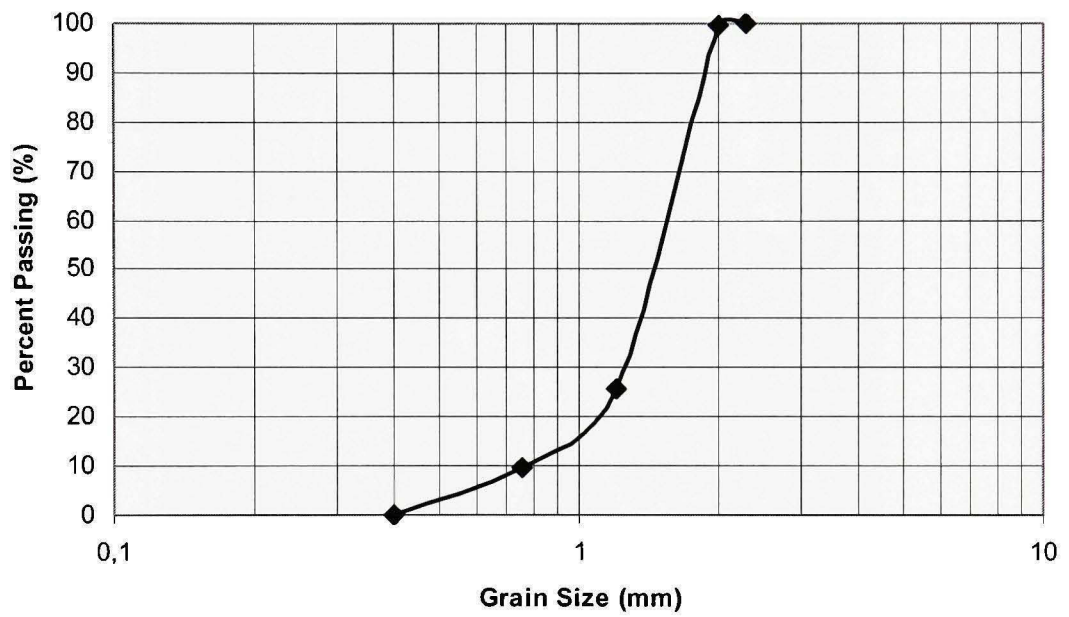
Figure 2.11 *Result of the sieve analysis.*
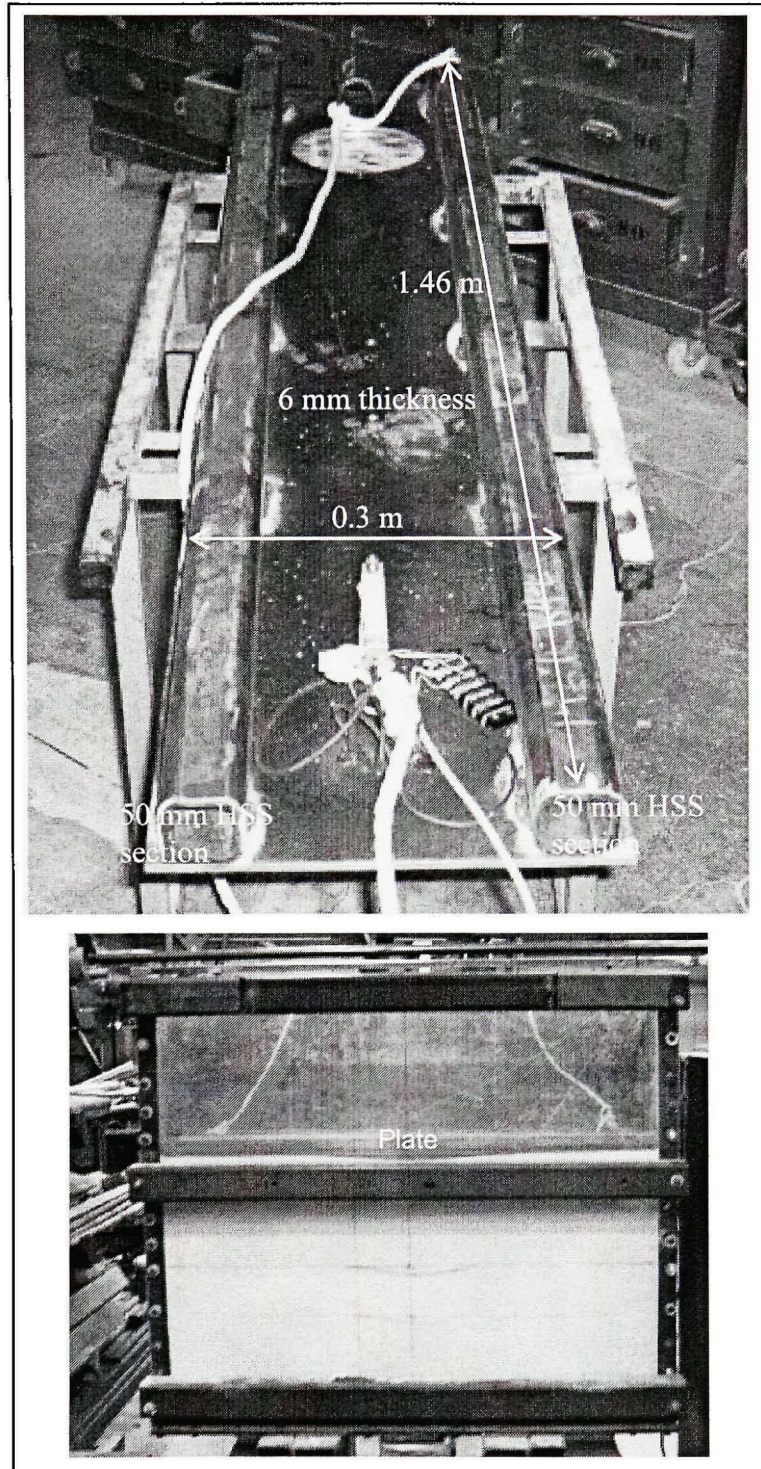
**Figure 2.12** *The rigid steel plate.*
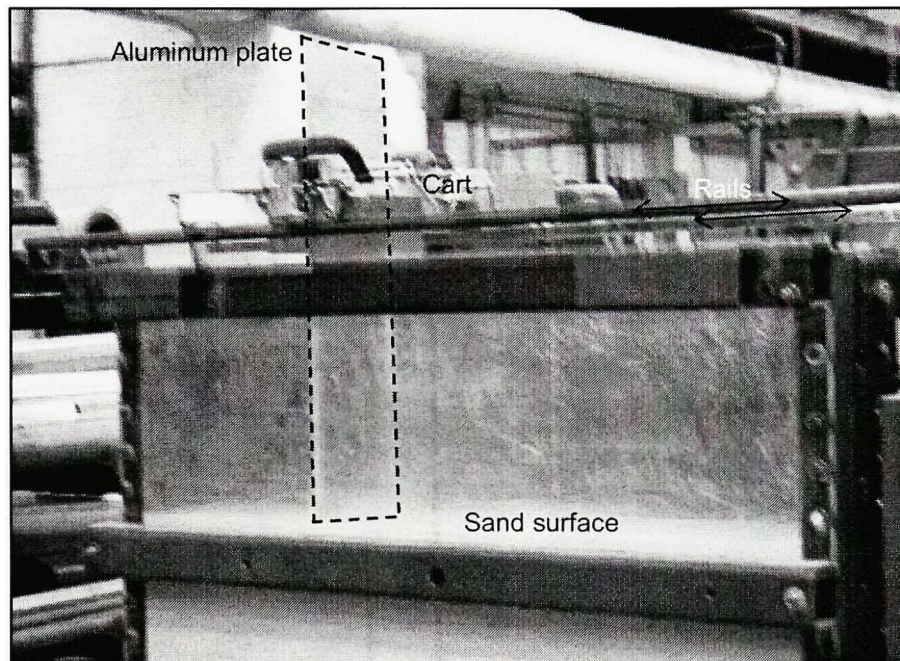
Figure 2.13 *Device to grade the sand.*
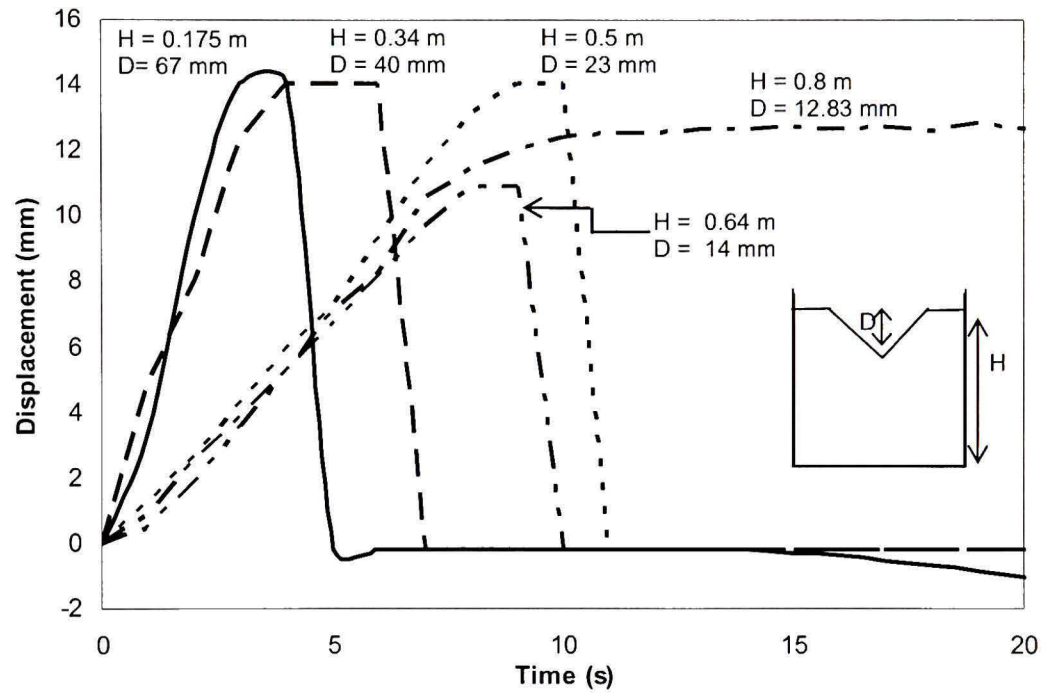
**Figure 2.14** *Displacement at the center line for the case of a free sand surface.*
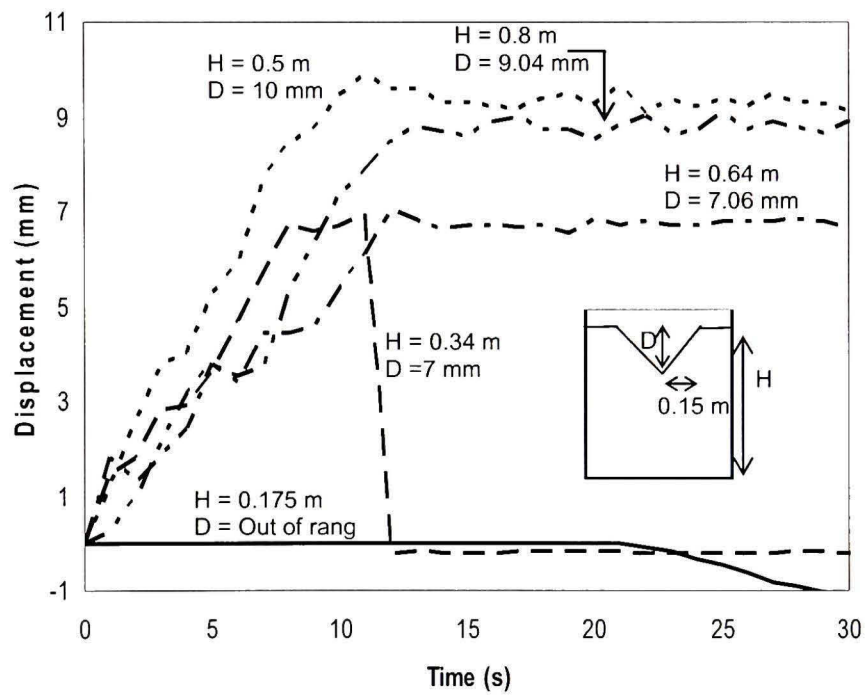
Figure 2.15 *Displacement at 0.15 m from the center line for the case of a free sand surface.*
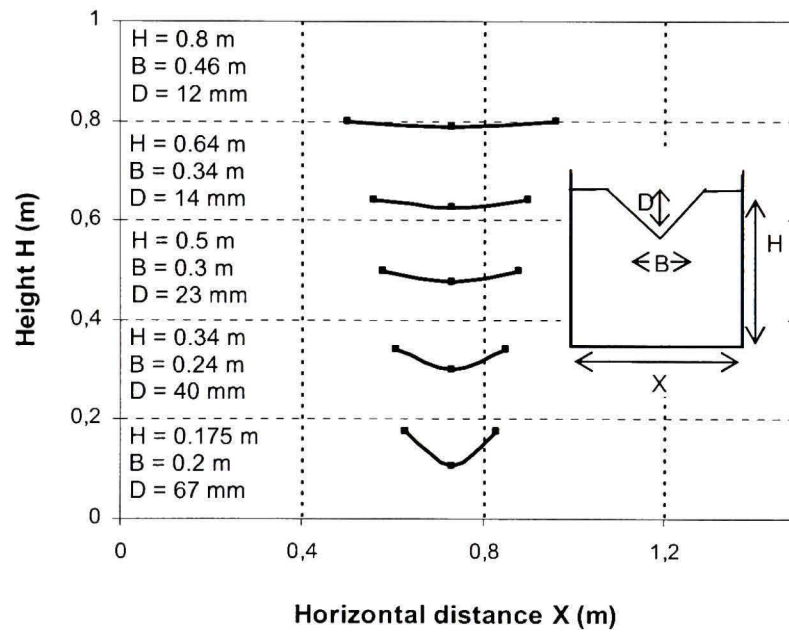
**Figure 2.16** *Settlement profile for the case of a free sand surface.*
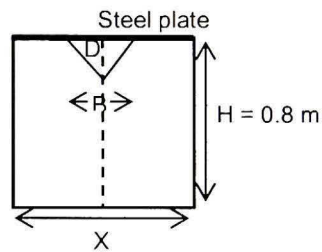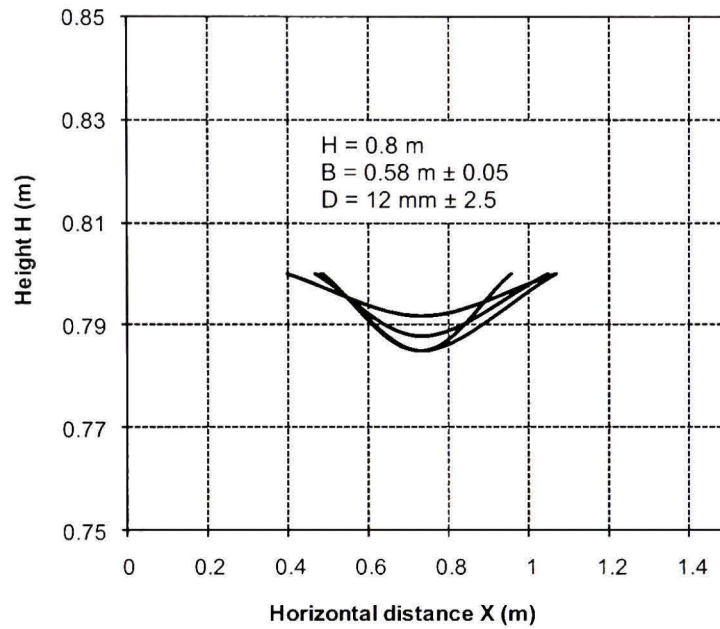
**Figure 2.17** *Settlement profile for the case of a loaded sand surface (repeatability tests).*
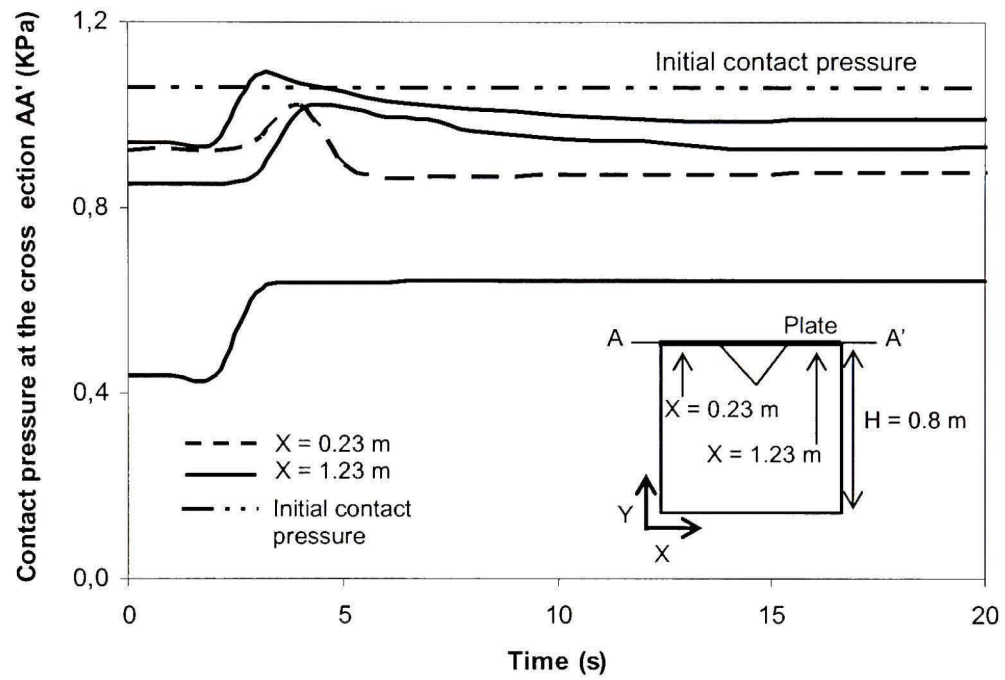
**Figure 2.18** *Contact pressure during the unloading process.*
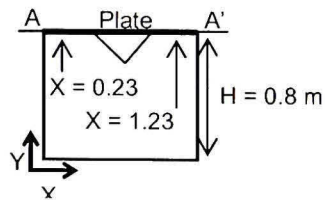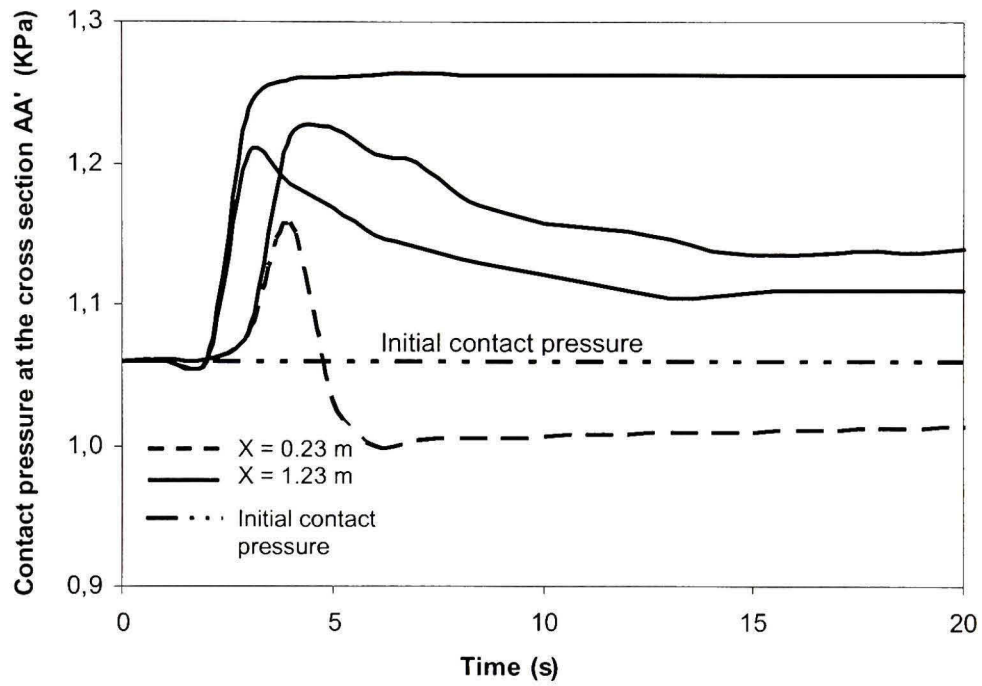
Figure 2.19 *Contact Pressure initiated from the same stage.*

CHAPTER 3

NUMERICAL ANALYSES

3.1   General

The finite element method has been applied to evaluate the effect of subsurface volume loss on the contact pressure and the tensile stresses developed in the lower fibers of a concrete slab-on-grade. The objectives are to calibrate a numerical model with the results obtained from the experimental program, and then analyze full scale scenarios. The numerical analyses were performed using Plaxis 8.6 finite element code for soils and rocks (Brinkgreve, 2001). In sections 3.2, 3.3 and 3.4 the details of the calibration process are presented, the strategy used to simulate soil erosion is described and the results are then discussed. Section 3.5 and 3.6 present the calibration and the physical model analyses. Section 3.7 presents the full scale analyses including the effects of the rigid boundary locations, the validation of the full scale model using analytical solutions and finally the results of a comprehensive parametric study are presented and discussed. The hypotheses made during the numerical analyses are stated at the end of section 3.7 for a better understanding.

3.2   Analysis details

Two parameters were recorded during the experimental program to calibrate the numerical model. Surface displacements for the free surface case, and vertical stresses (contact pressure) when the sand surface is subjected to uniform loading.

To simulate the sand movement out of the trap door, an attempt has been made using an approximate procedure that involves applying prescribed displacement at the bottom center line of the sand prism. A calibration was performed with respect to the resulting displacement at the surface (Figure 3.1). However, the prescribed displacements that have to

be assigned to the model were unrealistically large and therefore the calculation did not converge. Indeed, such prescribed displacements are physically meaningless according to the tank dimensions. It was concluded that the theory of continuum mechanic is not appropriate to model granular flow conditions; instead other methods such as the discrete element method can be used, which is beyond the scope of this project.

An alternative strategy has been adopted where the surface void (surface settlement) induced by the sand volume loss is directly applied at the surface (Figure 3.2). This approach allowed the incremental growth of the settlement through employing the excavation function of the finite element method. The stress redistribution at the loaded surface is used to calibrate the numerical model with the results obtained from the experimental program.

In Plaxis 8.6 the numerical simulation is initiated by subjecting the soil to an initial state of stress. The coefficient of lateral earth pressure at rest Ko is related to the internal friction angle by:

$$Ko = 1\text{-}sin\varphi \quad \text{(Jacky, 1944)} \tag{3.1}$$

The sand surface loading is activated first and then the surface void is simulated by deactivating the soil cluster (excavation) beneath the plate element.

3.3   Pre-processing

A plane strain finite element is used to model the rigid tank holding the sand prism and the steel plate. The boundary conditions were selected such that the vertical boundaries are fixed from movement in the horizontal direction (smooth rigid) and the horizontal boundaries fixed from movement in both directions (rough rigid). 15-nodded triangular solid elements were used throughout the analyses with a total number of 1941 elements (Figure 3.3). Line 1-2 is used to indicate the zone were the mesh is refined.

The surface void induced by the sand volume loss was approximated to a triangle (Figure 3.3, view A). This approximation was found to not affect the results since only the response along the contact plate/surface (above the void) is analyzed. As mentioned previously in Chapter 2, the surface void is identified by its horizontal width B and its vertical depth D. The surface void profile used in the analysis is based on the laboratory observations.

3.4   The constitutive models

Only the relevant parameters are defined in this section. For more information, the reader can refer to the list of symbols.

a) Steel plate

The steel plate was modeled using an element of flexural rigidity (EI) and normal stiffness (EA), where E, A and I are respectively the Young modulus, the normal section and the inertia. The plate is considered in these analyses as a rigid elastic material because of the small deformations it experiences. No weight has been attributed; instead a uniform distributed load was applied along its length.

b) Sand material

For dry sand the hardening soil model (Shanz, 1999) implemented in Plaxis V.8 is used. This model simulates soft and stiff soil when the stiffness has to be described much more accurately. Plastic strain due to both shear hardening and compression hardening are modeled. The yield surface has the hexagonal shape of the Mohr-Coulomb failure criterion in the principal stress space. The criterion includes also a yield cap that controls the plastic volume strain. The behavior is non-linear elastic within the yield surface whereas the hardening occurs when the state of stress reaches the failure surface.

- The hardening soil model assumes, in primary triaxial loading, a hyperbolic relation between the vertical strain ε_1 and the deviatoric stress q, as formulated by Duncan and Chang (1970). However the model uses the theory of plasticity rather than the theory of elasticity used in the original hyperbolic model.

The hyperbolic relationship plotted in Figure 3.4 can be described by:

$$\varepsilon_1 = \frac{1}{2E_{50}} \frac{q}{1-q/q_a} \quad \text{for: } q < q_f \tag{3.2}$$

q, ε_1 and q_a are respectively the deviatoric stress, the vertical strain and the asymptotic deviatoric stress derived from the Mohr-Coulomb failure criterion. The ultimate deviatoric stress, q_f, is given by:

$$q_f = (c\cot\varphi - \sigma_3')\frac{2\sin\varphi}{1-\sin\varphi} \quad \text{and} \quad q_a = \frac{q_f}{R_f} \tag{3.3}$$

c, φ and σ_3' are the cohesion, the friction angle and the minor principal stress, respectively. R_f is a failure ratio and a value of 0.9 is a suitable default setting (Plaxis-Material models manual, 2001).

- The tangent modulus within the primary loading is defined by a confining stress dependent stiffness modulus (E_{50}) defined by:

$$E_{50} = E_{50}^{ref}\left(\frac{c\cos\varphi - \sigma_3'\sin\varphi}{c\cos\varphi + p^{ref}\sin\varphi}\right)^m \tag{3.4}$$

where E_{50}^{ref} is a reference stiffness modulus corresponding to a reference confining pressure p^{ref} with a default setting of $p^{ref} = 100$. "m" is the stiffness stress dependency and a value of 0.5 is typical for sands and silts (Janbu, 1963). σ_3' is a confining pressure in a triaxial test.

- For unloading and reloading stress paths, the model uses a stress dependent stiffness elastic modulus (E_{ur}) defined by:

$$E_{ur} = E_{ur}^{ref} \left(\frac{c \cos \varphi - \sigma_3' \sin \varphi}{c \cos \varphi + p^{ref} \sin \varphi} \right)^m \tag{3.5}$$

where E_{ur}^{ref} is the reference Young modulus for unloading and reloading corresponding to the reference confining pressure P^{ref}.

For a one dimensional compression, the oedometer stiffness E_{oed} is defined by the equation below where E_{oed}^{ref} is a tangent stiffness at vertical stress of $-\sigma_1 = p^{ref}$ as shown in Figure 3.5.

$$E_{oed} = E_{oed}^{ref} \left(\frac{c \cos \varphi - \sigma_3' \sin \varphi}{c \cos \varphi + p^{ref} \sin \varphi} \right)^m \tag{3.6}$$

- The model's yield function is defined by:

$$f = \overline{f} - \gamma^p \tag{3.7}$$

$\overline{f}$ is a function of stress, composed by a plastic and an elastic component:

$$\overline{\overline{f}} = \frac{1}{E_{50}} \frac{q}{1 - q/q_a} - \frac{2q}{E_{ur}} \qquad (3.8)$$

γ^p is the hardening parameter:

$$\gamma^p = -\left(2\varepsilon_1^p - \varepsilon_v^p\right) \qquad (3.9)$$

Where ε_1^p and ε_v^p are the axial and the volumetric plastic strain, respectively.

- The relation between the rate of plastic volumetric strain $\dot{\varepsilon}_v^p$ and the rate of plastic shear strain $\dot{\gamma}^p$ is governed by the flow rule :

$$\dot{\varepsilon}_v^p = sin\,\psi_m\,\dot{\gamma}^p \qquad (3.10)$$

Where ψ_m is the mobilized dilatancy angle given by:

$$sin\,\psi_m = \frac{sin\,\varphi_m - sin\,\varphi_{cv}}{1 - sin\,\varphi_m\,sin\,\varphi_{cv}} \qquad (3.11)$$

in which φ_{cv} and φ_m are the critical friction angle and the mobilized friction angle respectively:

$$sin\,\varphi_m = \frac{\sigma_1 - \sigma_3}{\sigma_1 + \sigma_3 - 2c\,cot\,\varphi} \qquad (3.12)$$

The above equations are known as the stress-dilatancy theory (Rowe 1962, Rowe 1971) which state that the material tends to contract for $\varphi_m < \varphi_{cv}$ and dilate for $\varphi_m > \varphi_{cv}$. At failure when the mobilized friction angle φ_m is equal to the failure angle φ, we can write from equation 3.11 that:

$$sin\,\varphi_{cv} = \frac{sin\,\varphi - sin\,\psi}{1 - sin\,\varphi\,sin\,\psi} \qquad (3.13)$$

- The plastic volume strain in isotropic compression is defined in the hardening soil model by a cap yield surface that closes the elastic region. The function is given by:

$$f^c = \frac{\tilde{q}}{\alpha^2} + p^2 - p_p^2 \qquad (3.14)$$

Where:

α is an auxiliary parameter related to the normally consolidated coefficient of lateral earth pressure at rest K_0^{nc}.

$$P = \frac{\sigma_1 + \sigma_2 + \sigma_3}{3} \qquad (3.15)$$

$$\tilde{q} = \sigma_1 + (\delta - 1)\sigma_2 - \delta\sigma_3 \quad with \quad \delta = \frac{3 + sin\,\varphi}{3 - sin\,\varphi} \qquad (3.16)$$

P_p is the isotropic preconsolidation stress.

Figures 3.6 and 3.7 depict both the shear and the cap yield surface in the $\tilde{q} - p$ plane and the principal stress space.

- The stiffness properties of the sand were assigned based on the values proposed by Kempfert and Gebreselassie (2006) for σ'_3/P^{ref} of about 0.10 as shown in Figure 3.8. The sand and plate material properties are listed in Table 3.1 below.

Table 3.1

Soil and plate parameters

Soil parameters		Plate Parameters	
Material model	Hardening soil model	Material model	Elastic
Type of behavior	Drained	EA (kN/m)	$2,88 \ 10^9$
Soil unit weight (kN/m³)	14	EI (kNm²/m)	9999
c (kPa)	10^{-3}	d (m)	$6,46 \ 10^3$
φ (°)	30	W (kg)	0
Ψ (°)	0	υ	0,3
E_{50}^{ref} (kPa)	$2 \ 10^4$	Load (kN/ m²)	-1.06
E_{eud}^{ref} (kPa)	$2 \ 10^4$		
E_{ur}^{ref} (kPa)	$6 \ 10^4$		
m	0,5		
υ_{ur}	0,2		
P^{ref} (kPa)	100		
K_0^{nc}	0,5		
R_f	0,9		

3.5   Calibration of the model

The analysis conducted using the hardening soil model allowed for the calculation of the vertical stresses at the interface between the plate and the solid after the excavation procedure. Figure 3.9 shows the redistribution of the vertical stresses over the horizontal distance for a surface void of a width B = 0.58 m. In addition, the experimental measurements taken at two specific locations (X = 0.23 m and X = 1.23 m) are also plotted. It can be seen at the specific locations, that the calculated stresses (1.14 kPa) are in good agreement with those measured (1.26 kPa, 1.22 kPa, 1.21 kPa and 1.16 kPa). A difference of 5.78% between the calculated stresses and the mean value of the measured stresses is observed. The vertical stresses before excavation (initial contact pressure) are displayed in Figure 3.9 as well. A pressure increase of 17% at the specific locations was observed after the excavation procedure.

3.6   Physical model analyses

Once the model was calibrated, a series of analysis were performed to simulate the experimental setup. The analysis involved cases where the size of the void is incrementally increased (width B), and its location is varied to examine the two cases of centered and off-centered surface voids. Figures 3.10 and 3.11 illustrate the contact pressure from five different void sizes (B = 0.1 m, B = 0.2 m, B = 0.3 m, B = 0.4 m, B = 0.58 m). For the case of a centered void, stresses experience a big drop at the two extremities of the width B. An increase of up to 40% from the initial contact pressure was reached for a distance B = 0.58 m. This sudden increase in stresses can be explained by the transition from a zone where the solid cluster was deactivated to simulate the void, to a zone where the solid still exists. The stresses started to decrease after reaching a peak. For the first three void sizes, the stresses decreased until they stabilized around a value close to the initial contact pressure. However, for the void size of B = 0.4 m, the stresses reached a value of approximately 14% less than the initial contact pressure. For B = 0.58 m, the contact pressure decreased quasi-uniformly until zero. It appears that there is a critical width B between 0.4 m and 0.58 m for which the

stresses never coincide with the initial contact pressure and are redistributed all along the still plate.

A similar mechanism develops for the off-centered voids. The contact pressures are slightly more important at the peaks compared to the centered cases. The pressure corresponding to the five void widths reaches the initial value at the same distance from the void boundaries.

3.7   Full scale analyses

Full scale analyses involved the replacement of the thin plate element used in the calibration section by a thick concrete slab-on-grade. To simulate the external loading, the concrete slab is subjected to, a uniformly distributed load equivalent to that induced by snow trucks was prescribed over a distance of 0.2 m, which corresponds to a tire width. The effect of the boundaries location has been investigated to find the optimum distance to the rigid boundaries. In addition, the model has been validated by analyzing a benchmark problem. The concrete slab-on-grade (150 mm thick and 1.60 m wide) is modeled as an elastic material with a Young modulus of 27 GPa and a Poisson ratio of 0.2. The interface between the slab and the sand is controlled in the program by a reduction factor (R_{int}) that relates the strength of the slab to the strength of the sand. This factor was found to not have significant influence on the results and was then taken as $R_{int} = 1$. The Young modulus is estimated using the equation below given by the American Concrete Institute.

$$E = 4700W^{1.5}\sqrt{f_c}$$ (3.17)

Where f_c is the compressive strength of the concrete taken as 32 MPa and W is the unit weight (22.86 kN/m^3).

The hypotheses made during the numerical analyses are:

a- A plane strain finite element model have been used during the analyses, although subsurface voids are most likely three dimensional.

b- Truck loads are considered to be three dimensional in nature, however, to simplify the analyses; strip loads varying from -20 kPa to -140 kPa were applied.

c- The different sizes of void (local loss of support) underneath the slab were based on the results obtained from the experimental program and therefore are not representative.

3.7.1   Effect of boundary locations

In order to eliminate the influence of the lateral boundaries on the numerical results, a parametric study was conducted where the boundaries are moved horizontally away from the concrete slab. Figure 3.12 and 3.13 show the geometry selected after several trials and errors. The analysis was calculated for the worst conditions, with the highest load and the larger surface void. It was found that a distance of 7 m away from the concrete slab in the lateral direction and 4 m in the vertical direction correspond to an insignificant change in displacements and therefore was adopted in the present analysis.

3.7.2   Validation of the full scale model with known analytical solutions

The performance and accuracy of any numerical calculation must always be tested by carrying out analysis of problems with known analytical solutions. This validation adds confidence before using more sophisticated models. Therefore, an elastic simulation was conducted to analyze a rigid strip footing applying a uniform vertical load and supported by an elastic soil. The analytical solution to this problem is given by Girould (1973).

Figure 3.14 shows the relevant soil data used in the analysis. A uniform load of -300 kPa is applied at the soil surface and the settlement calculated from the results of the finite element simulation. The vertical displacement distribution underneath the loading at the end of the finite element analysis is shown on Figure 3.15. The settlement profile was calculated to have a maximum value of 10.64 mm at the center and 7.376 mm at the edges.

The analytical solution given by Girould (1973) is given by:

- Settlement at the load center line

$$S = \frac{2aP}{E} P_H \qquad (3.18)$$

With $P_H = 1.33$ for $\beta = \dfrac{H}{2a} = 5$

- Settlement at the edges

$$S = \frac{2aP}{E} P_H \qquad (3.19)$$

With $P_H = 0.925$ for $\beta = \dfrac{H}{a} = 2.5$

In the above equations, we have:

S : Settlement.

H : Soil thickness.

2a : Footing width.

P : Uniform load.

E : Soil Young modulus.

P_H: Dimensionless coefficient depending on υ and β, given by a chart (Girould, 1973).

β : Relative soil thickness.

For the geometry and material properties used in the finite element analysis, the analytical solutions calculated a settlement of 10.64 mm at the load center line and 7.4 mm at the edges. The difference between the numerical and the analytical solution is therefore insignificant.

3.7.3 Discussion of the full scale analyses

Several scenarios have been considered for the full scale analyses. The examined parameters are the position of the void beneath the slab (centered or off-centered) and the width of the void B (Figures 3.16 and 3.17). A maximum value of B = 0.58 m have been selected based on the results of the experimental program. The intensity of the prescribed load has been varied as well. It is worth mentioning that the truck load is considered to be three dimensional in nature, however, to simplify the analyses, a strip load varying from -20 kPa to -140 kPa was applied. These scenarios were run first with a minimum void depth of 0.02 m and a maximum depth of 0.067 m as measured in the experimental tests. A summary of the scenarios is schematically represented in Figure 3.18.

Case A: D = 0.02 m

The results of the analyses are summarized in Figures 3.19 and 3.20. The tensile stresses induced into the concrete slab are normalized with respect to an allowable ultimate tensile stress σ_{ult} of 1.6 MPa corresponding to 5% of the compressive strength. For the case of centered voids (Figures 3.19), the tensile stresses are proportional to the width B. The largest value corresponded to 87 % of σ_{ult} and was reached when a load of -100 kPa was applied for a width B = 0.58 m, and a load of -140 kPa for a width B = 0.1 m. For the latter load, the calculation did not converge and the program stopped before the end of the simulation. However, the trend of the curve let suppose that failure of the concrete can be reached for a width B around 0.17 m. We can also suppose according to the trend of the

curves corresponding to a load of -100 kPa, -60 kPa, -20 kPa, that σ_{ult} is reached for significantly large voids underneath the slab.

The trend presented in Figure 3.20 is completely different from the above. Indeed, when the void is off-centered the tensile stresses are constant until certain value of the width B, where the stresses start to decrease. Although the tensile strength of the slab was not exceeded, the soil experienced shear failure before the end of the numerical simulations except for a small load (-20 kPa). Based on this observation, the plastic points according to the Mohr-Coulomb yield surface, resulting from the presence of voids for a load of -140 kPa are plotted on Figures 3.21 and 3.22 before and after void development, respectively, for comparison. The Mohr-Coulomb plastic points were found to increase around the void where seemingly soil shear failure is taking place.

Case B: D = 0.067 m

Figure 3.23 shows the effect of the void width on the response of the slab-soil system with the maximum void depth obtained from the experimental program under the maximum load used in these analyses. For the cases of centered voids, no soil shear failure developed as opposed to the case A. However, excessive tensile stresses ($1.25\sigma_{ult}$) developed in the outer fibers of the concrete slab. For the off-centered void, the tensile stresses followed a similar trend and intensity as in Case A, except that soil shear failure occurred at a width B of 0.4 m while for the minimum depth, failure occurred for B = 0.58 m.

Figures 3.24 and 3.25 show an example of the vertical stress propagation for the centered and off-centered voids, respectively, under a prescribed load of -100 kPa. By inspecting the shape of the contour lines it can be seen that there is a depth (influence depth) where the presence of the void does not have an influence on the vertical stress distribution (the depth where the pressure bulb shape due to the presence of void vanish). The effect of the void on the vertical stress distribution is plotted in Figure 3.26. In general as the width of the void increases, the influence depth gets higher.

For the two cases, the influence depth extended to a distance that ranges from 0.3 m to about 1 m below the surface and was found to be more significant for off-centered voids than for centered-voids.

Another way of presenting the full scale analyses is to plot the normalized tensile stresses developed in the outer fibers of the slab versus the prescribed loads for a void width of $B = 0.3$ m (Figure 3.27). By inspecting the slope of the two curves, it can be seen that the rate of the tensile stresses developed in the slab is higher for the case of a centered void than for an off-centered void. A maximum value ranging between $0.70\sigma_{ult}$ and $0.78\sigma_{ult}$ was reached for both cases.
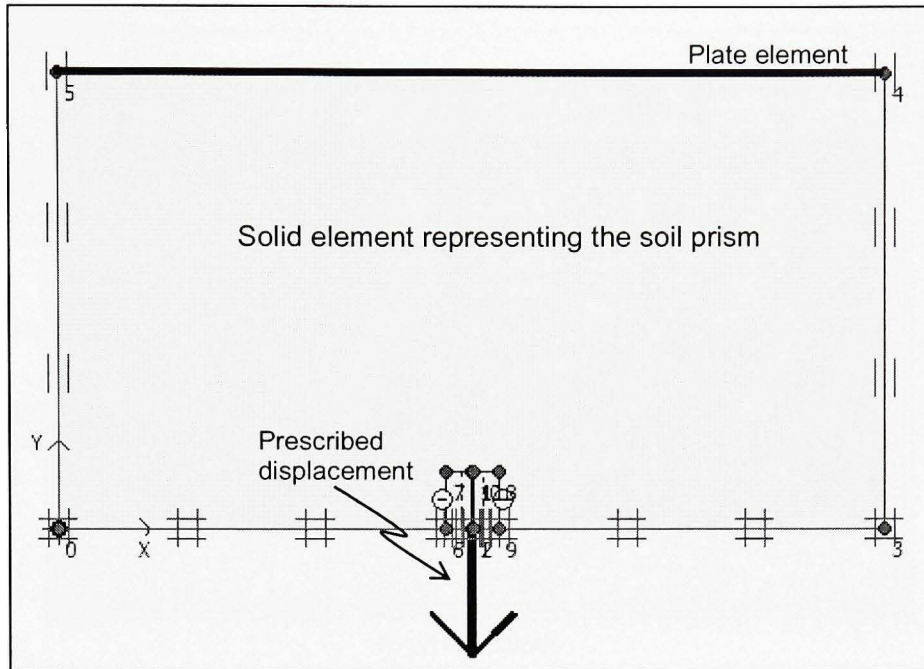
Figure 3.1 *Model with prescribed displacement.*
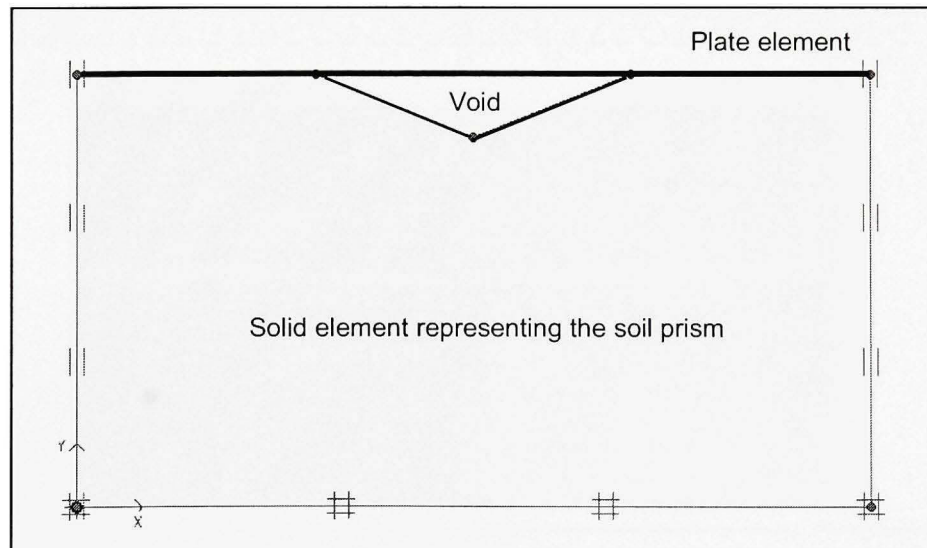
Figure 3.2 *Model with surface excavation.*
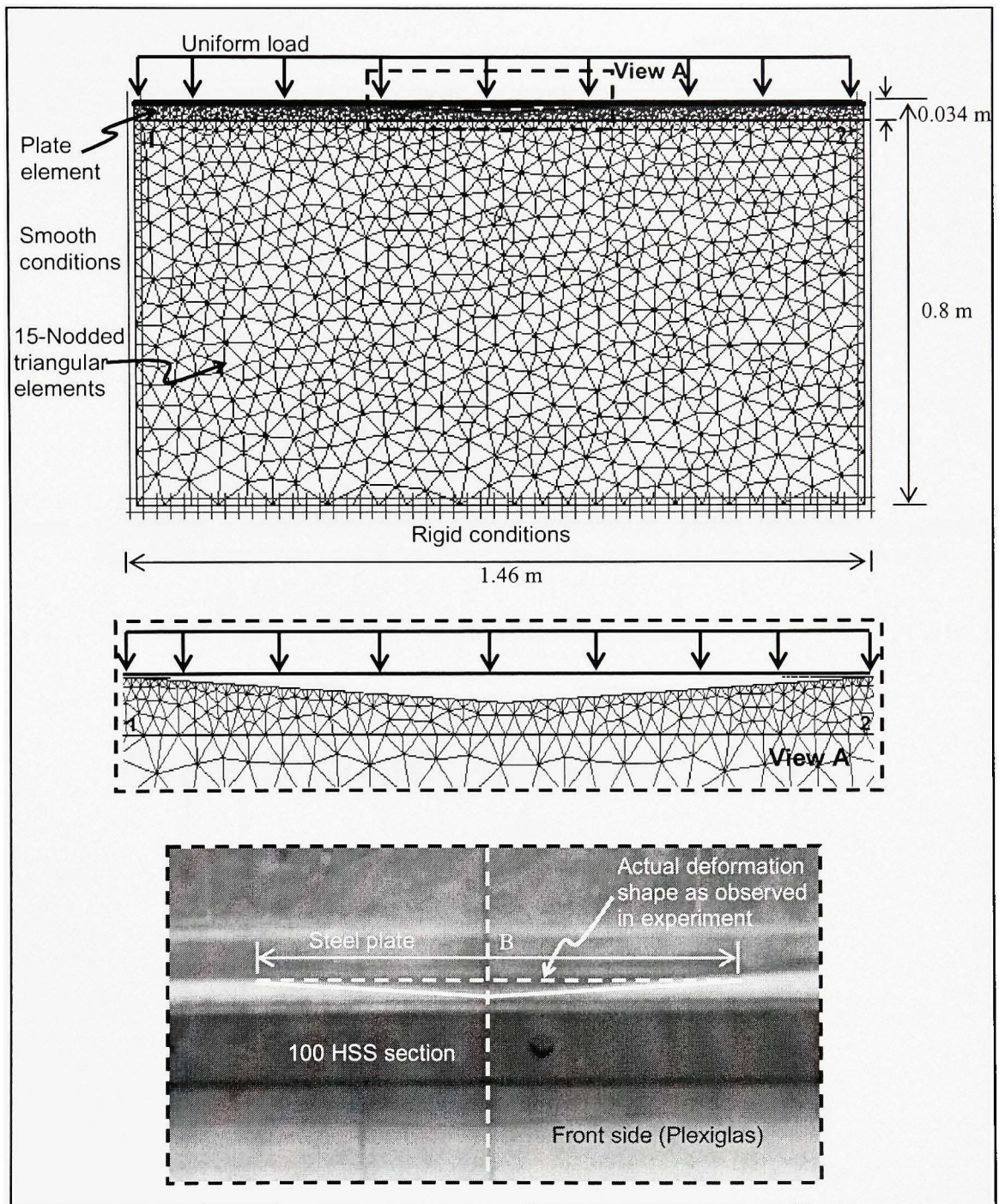
Figure 3.3 *Typical finite element mesh with 15–nodded triangular elements.*
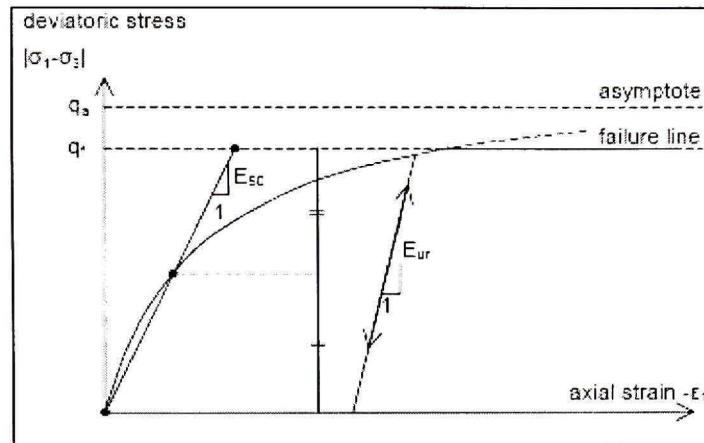
Figure 3.4 *Hyperbolic stress strain relation in primary loading*
(Plaxis, 2001)

Source: This figure was taken from the manual of the software Plaxis V8 (2001), *Material models manual: Hyperbolic stress strain relation in primary loading for a standard drained triaxial test,* p. 5-3.
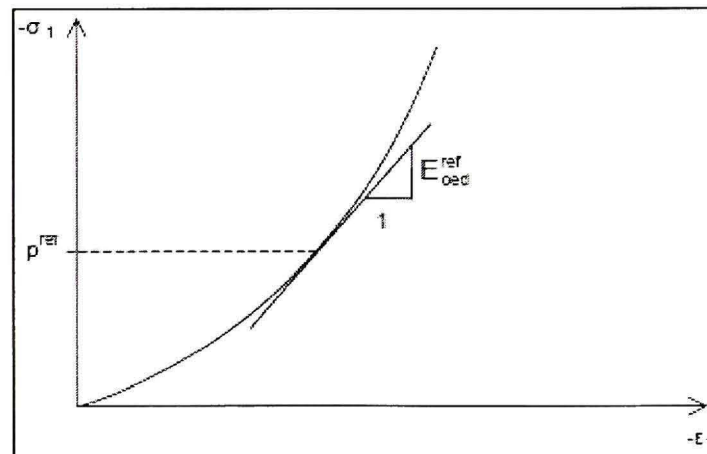
Figure 3.5 *Definition of* E_{oed}^{ref} *in isotropic compression test.*
(Plaxis, 2001)

Source: This figure was taken from the manual of the software Plaxis V8 (2001), *Material models manual: Definition of* E_{oed}^{ref} *in oedometer test results,* p. 5-9.
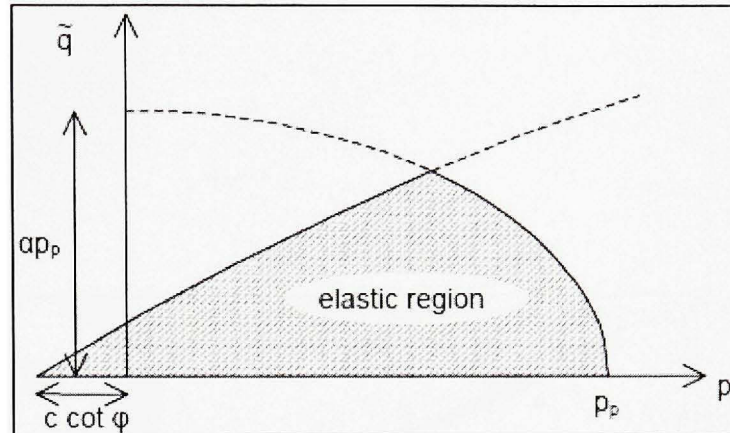
Figure 3.6 *Yield surface of the Hardening-Soil model in q-p plane.*
(Plaxis, 2001)

Source: This figure was taken from the manual of the software Plaxis V8 (2001), *Material models manual: Yield surface of the hardening soil model in q-p plane*, p. 5-13.
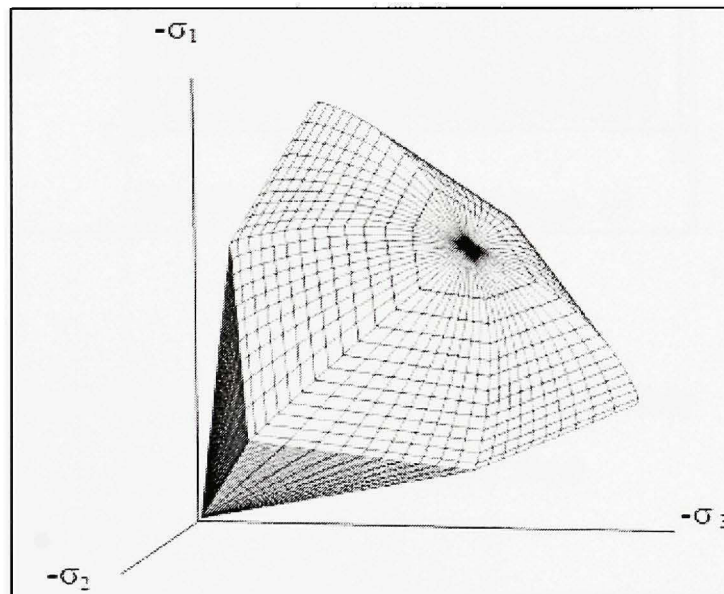
Figure 3.7 *Representation of the total yield contour in principal stress plane.*
(Plaxis, 2001)

Source: This figure was taken from the manual of the software Plaxis V8 (2001), *Material models manual: Representation of the total yield contour in principal stress space for cohesionless soil*, p. 5-13.
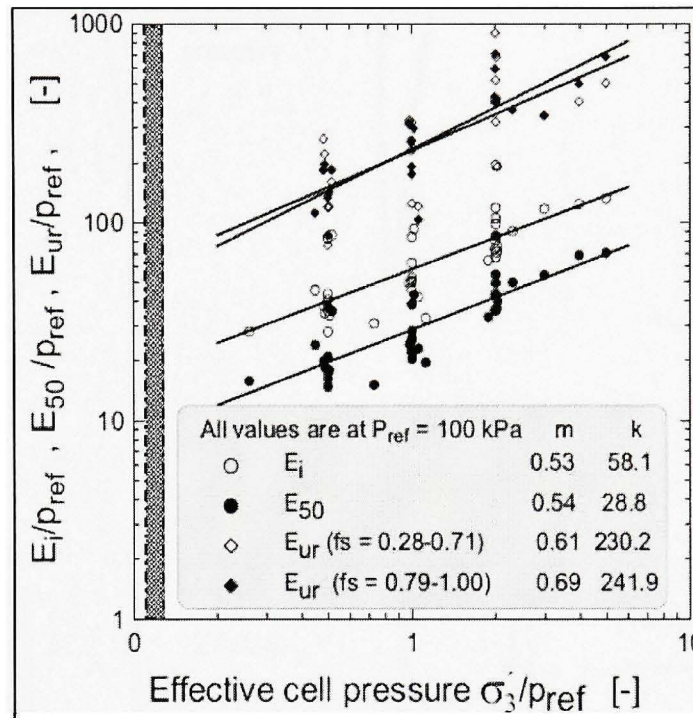
Figure 3.8 *The variation of the modulus of elasticity
with the confining pressure.*
(Kempfert and Gebreselassie, 2006)
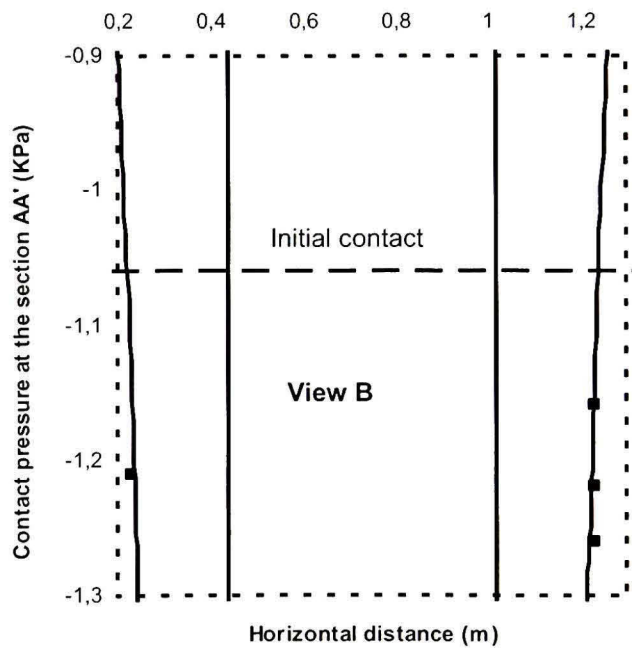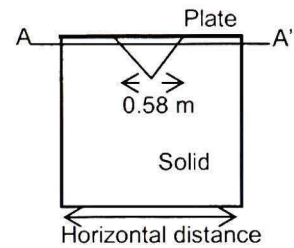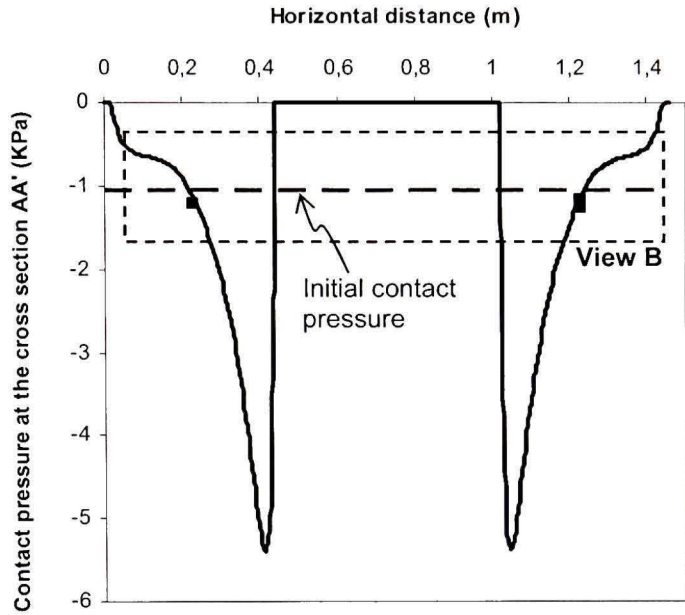
Figure 3.9 *Results of the calibration.*
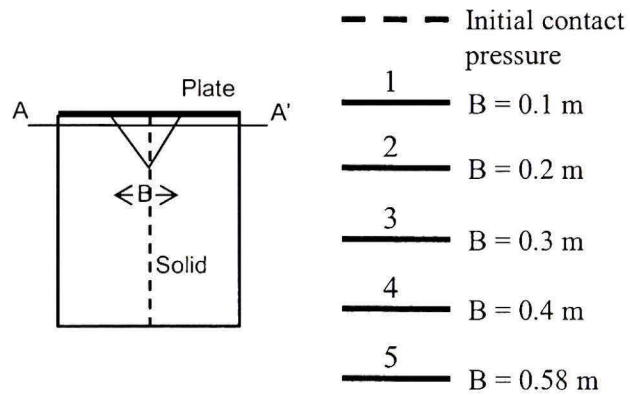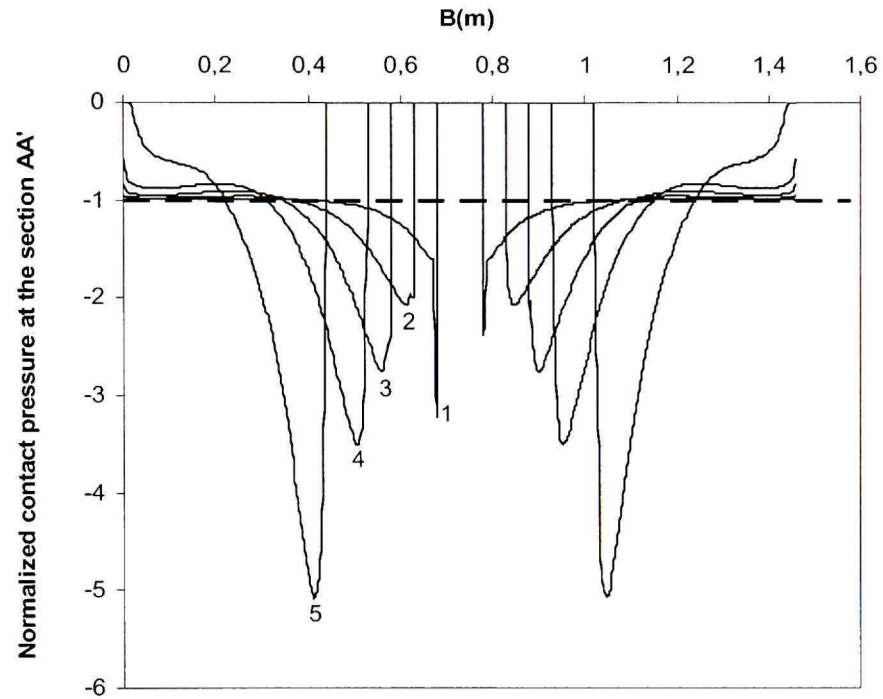
Figure 3.10 *Contact pressure for centered voids.*
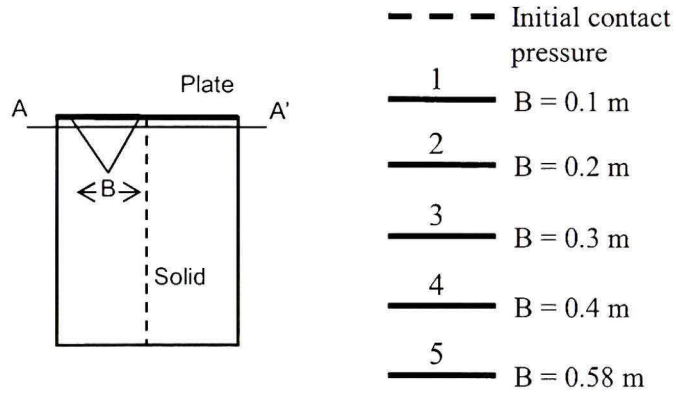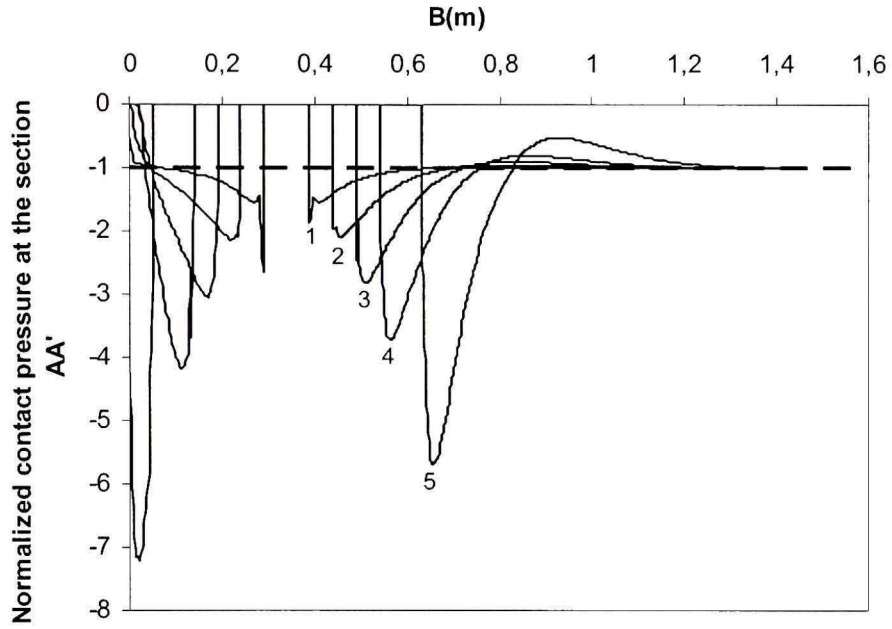
Figure 3.11 *Contact pressure for off-centered voids.*
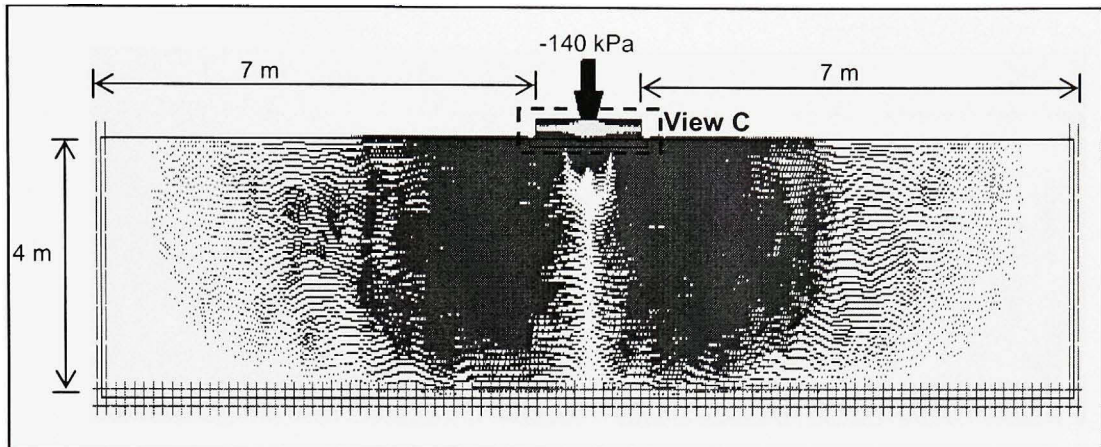
**Figure 3.12** *Effect of the boundary locations on the horizontal displacements.*
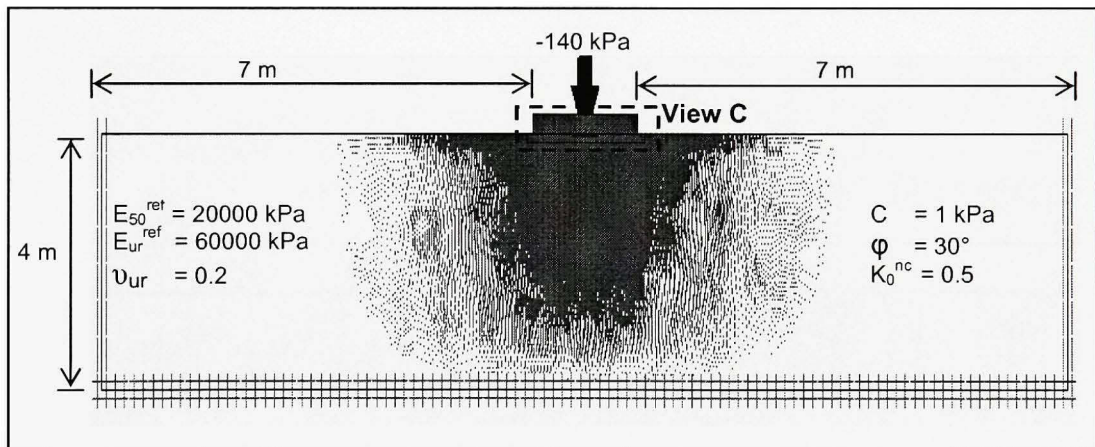
**Figure 3.13** *Effect of the boundary locations on the vertical displacements.*
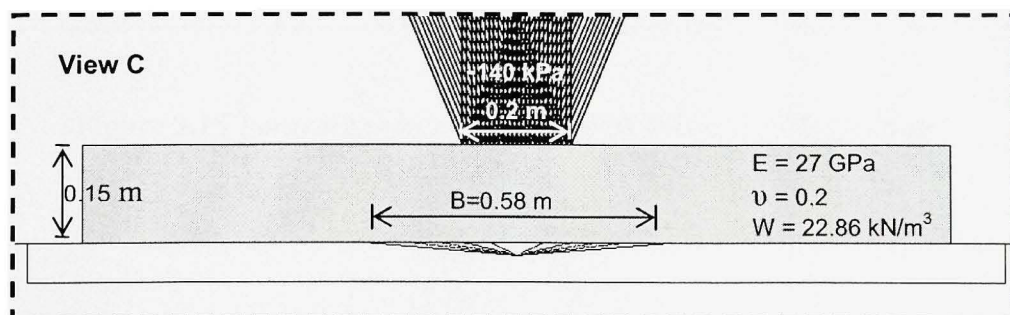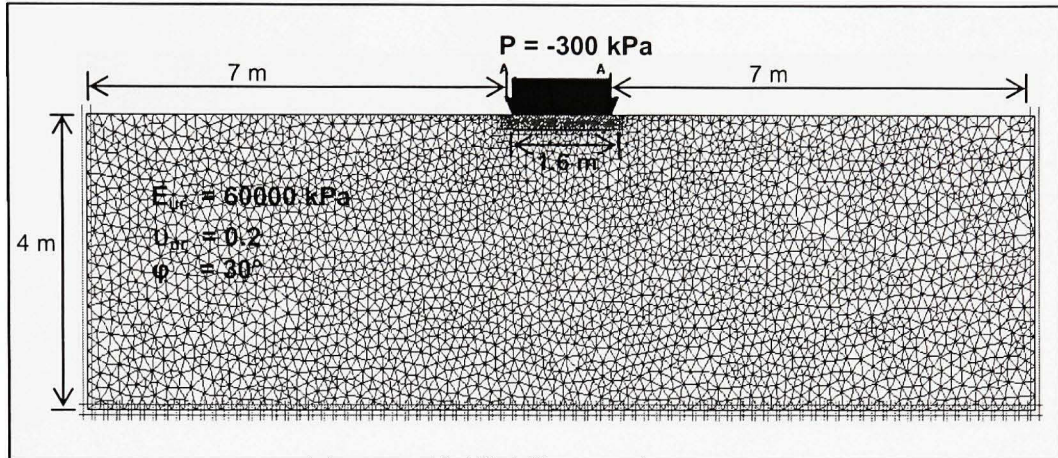
Figure 3.14 *Problem geometry.*
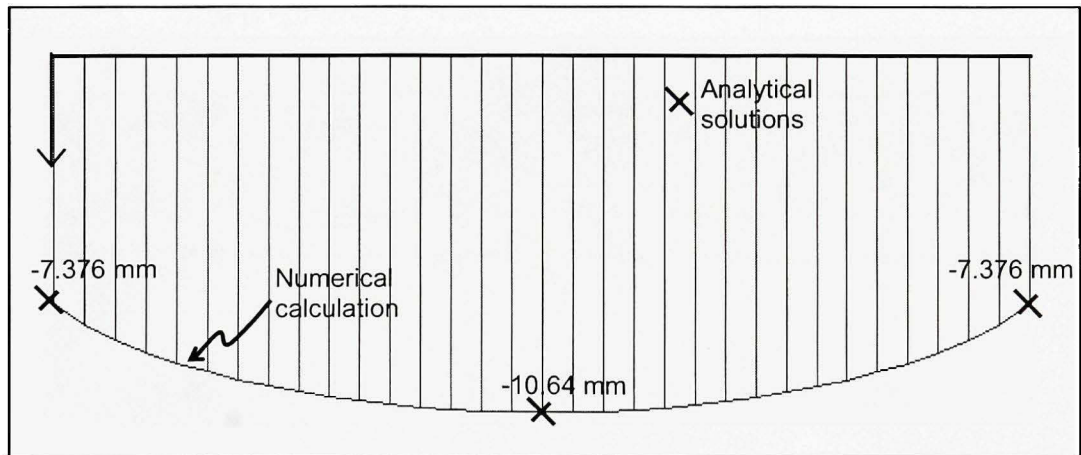
**Figure 3.15** *Vertical surface displacements induced by the footing.*
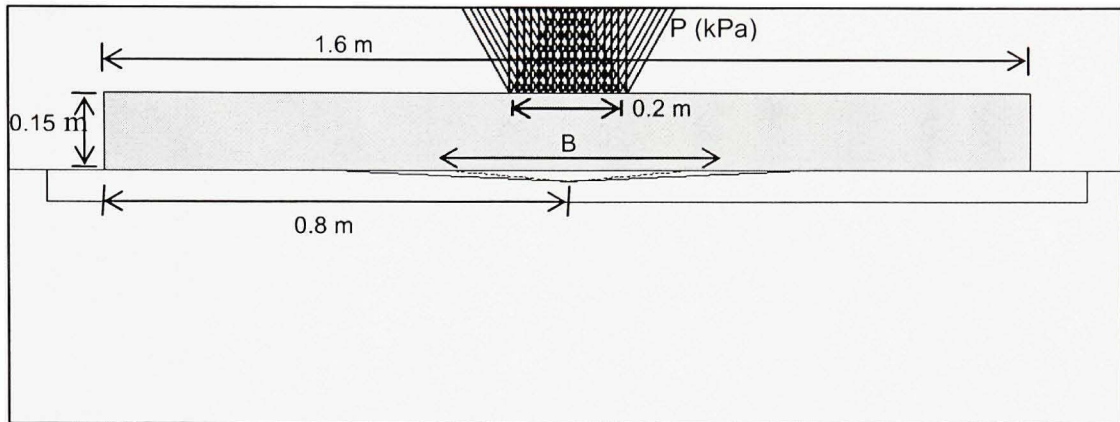
**Figure 3.16** *Geometry details for the case of the centered voids.*
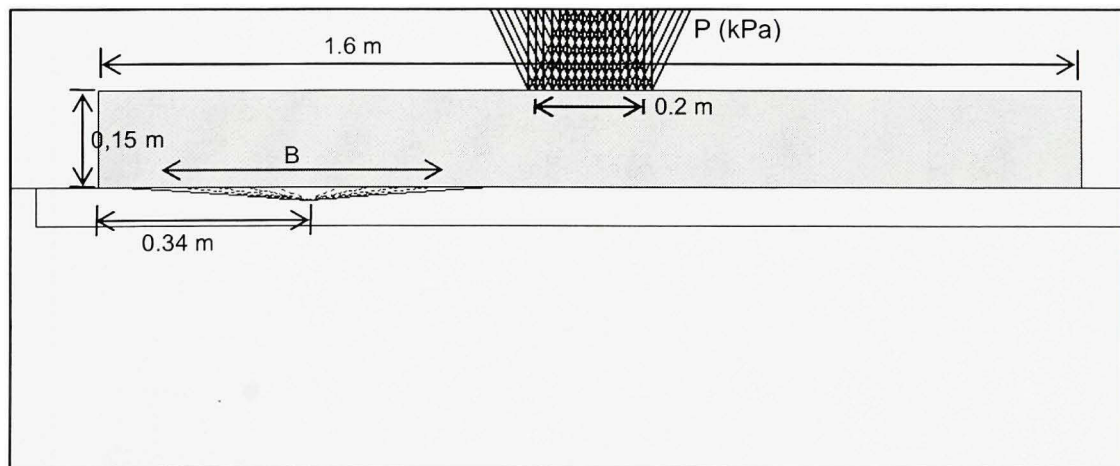
**Figure 3.17** *Geometry details for the case of the off-centered voids.*
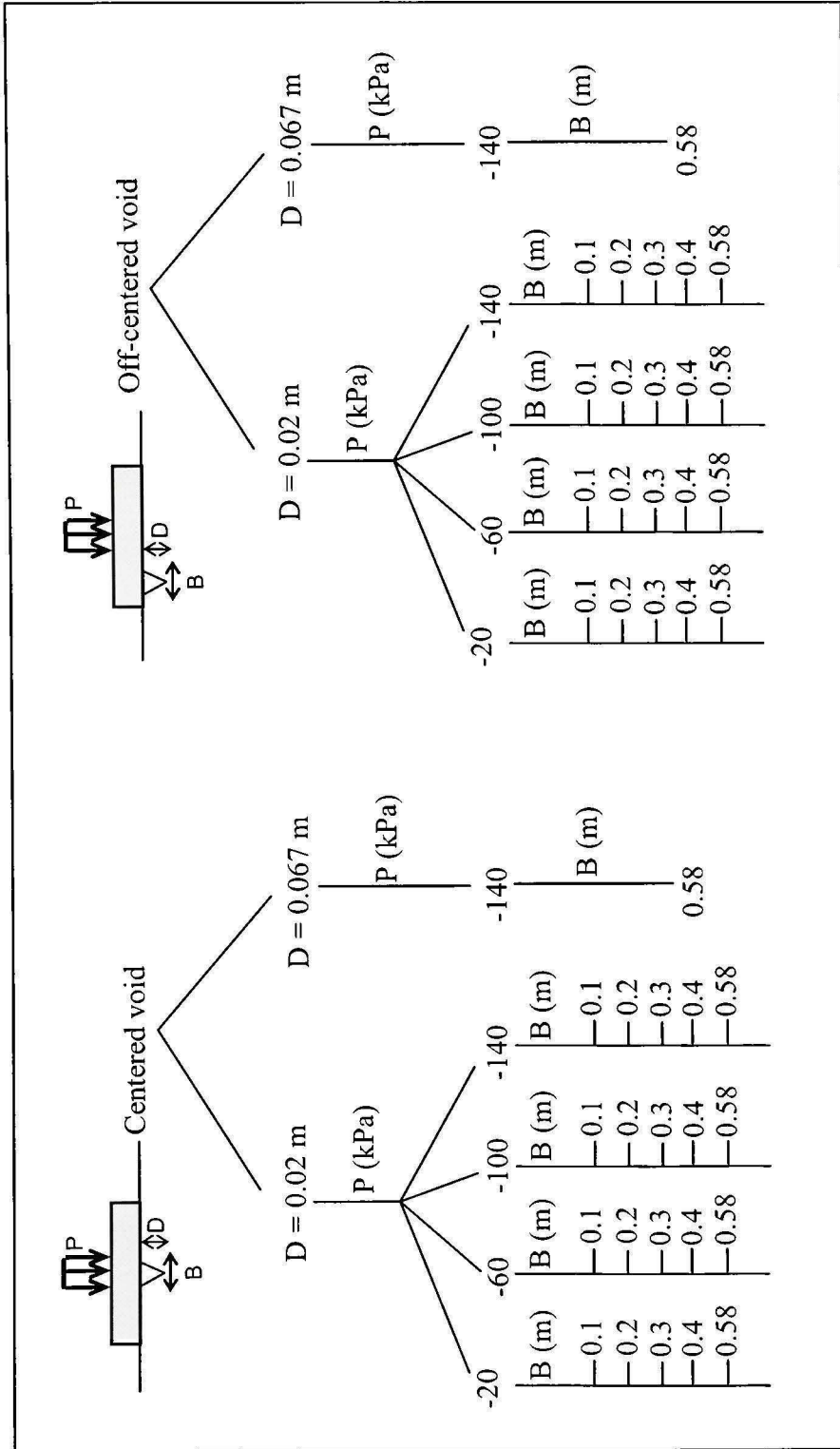
**Figure 3.18** *Plan of scenarios simulations.*
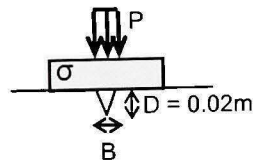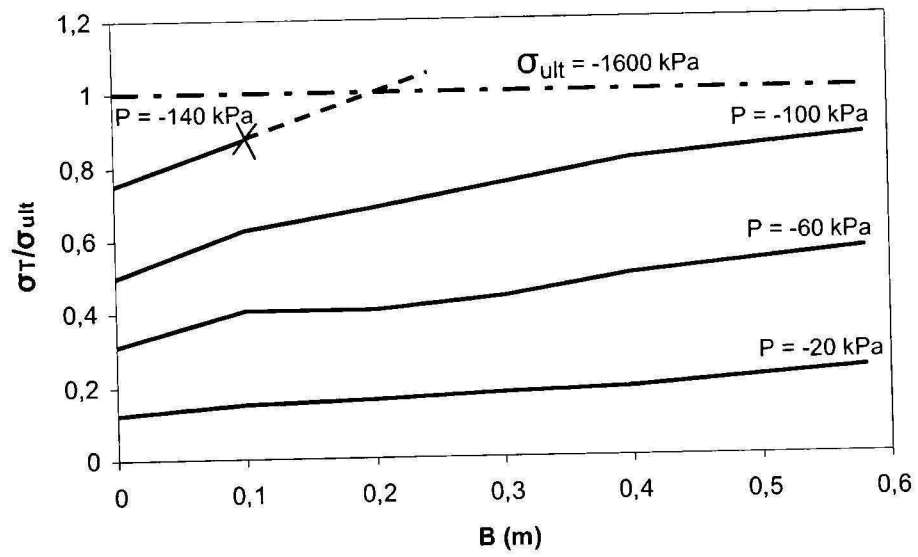
Figure 3.19 *Normalized tensile stresses induced into the concrete slab subjected to a uniform load and a centered void.*
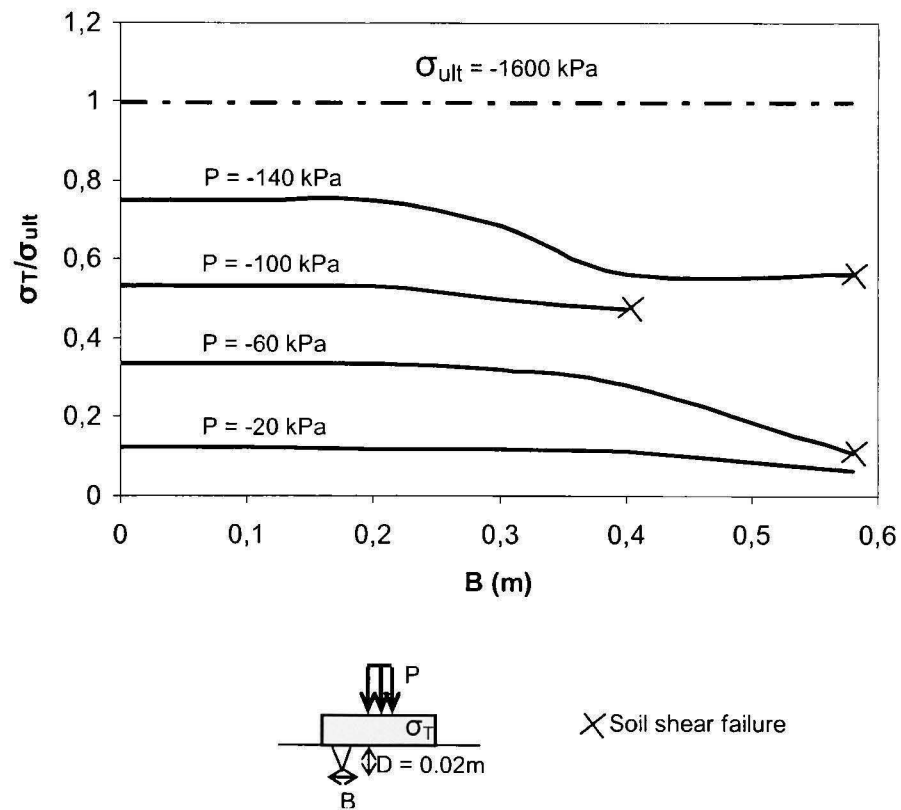
Figure 3.20 *Normalized tensile stresses induced into the concrete slab subjected to a uniform load and an off-centered void.*
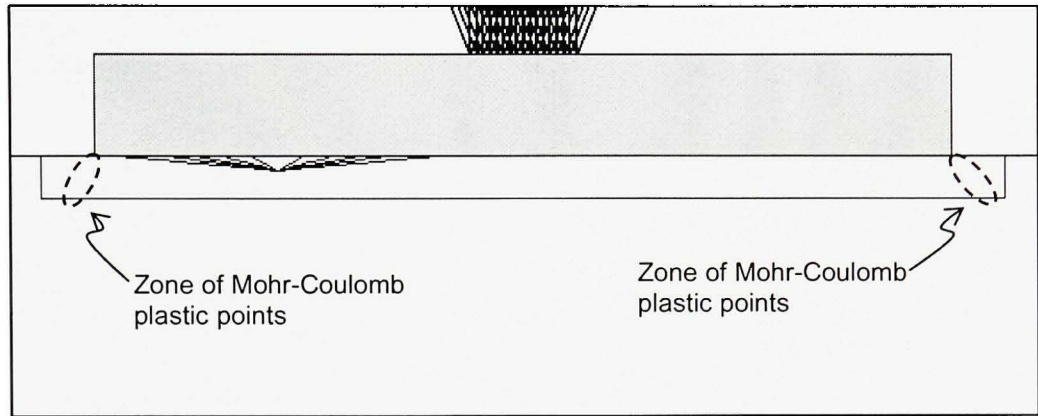
**Figure 3.21** *Mohr coulomb plastic points before presence of void.*
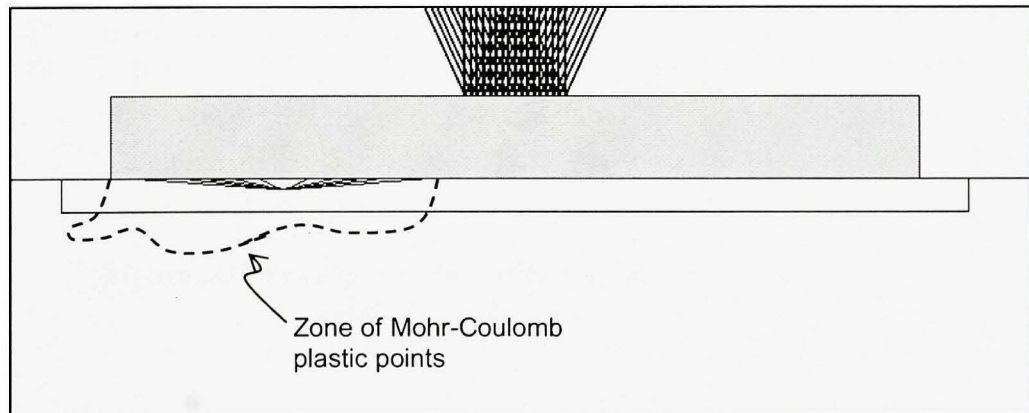
**Figure 3.22** *Mohr coulomb plastic points for a void width of B = 0.58 m.*
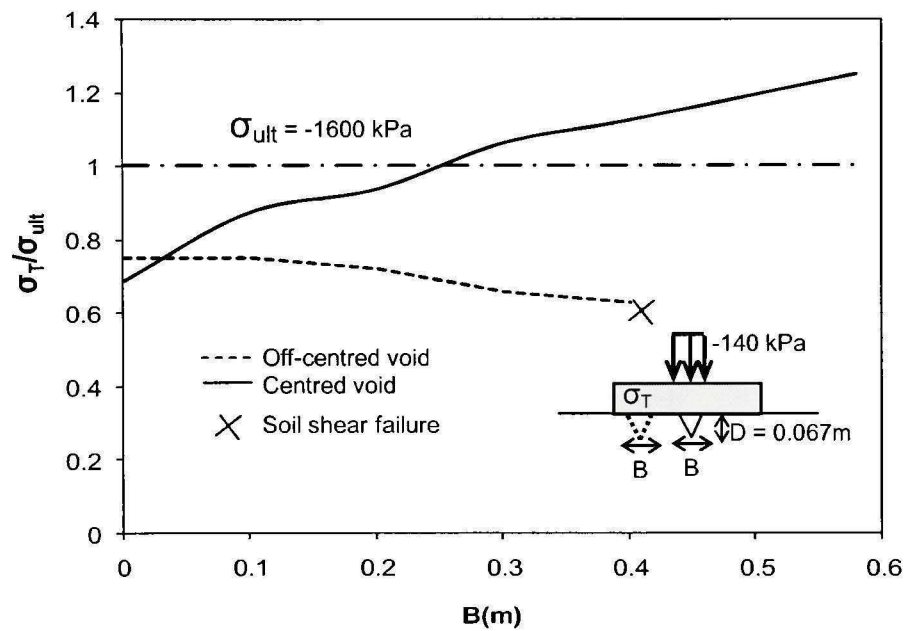
Figure 3.23 *Influence of the void depth on the tensile stresses induced into the concrete slab.*
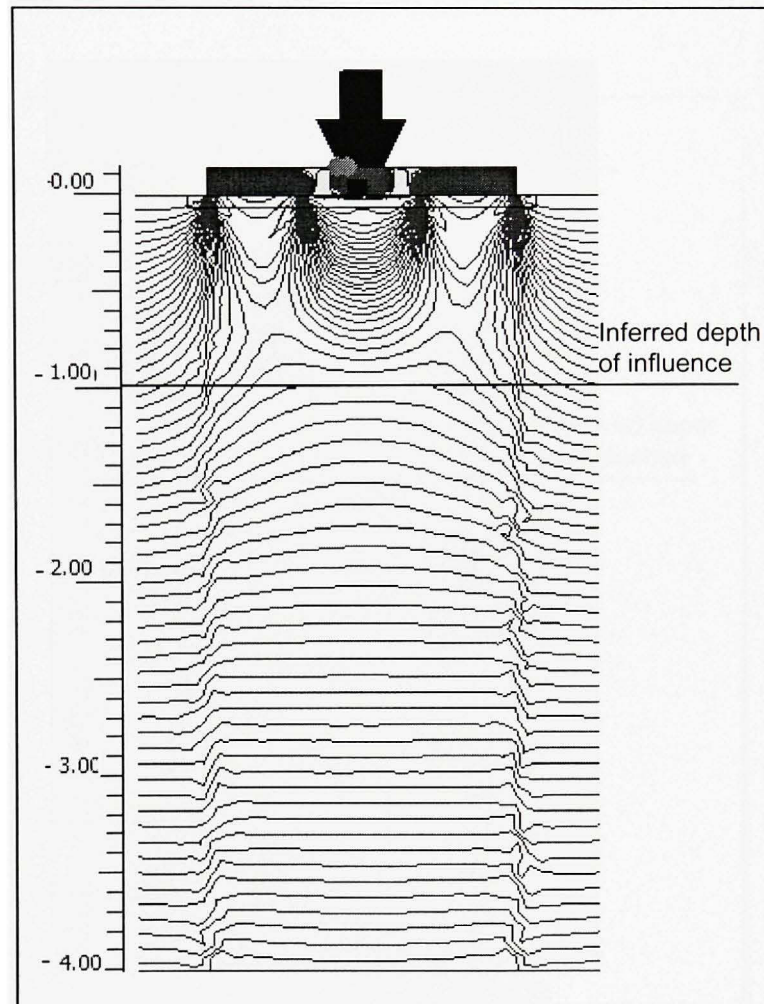
Figure 3.24 *Influence of the centered void on the vertical stress distribution.*
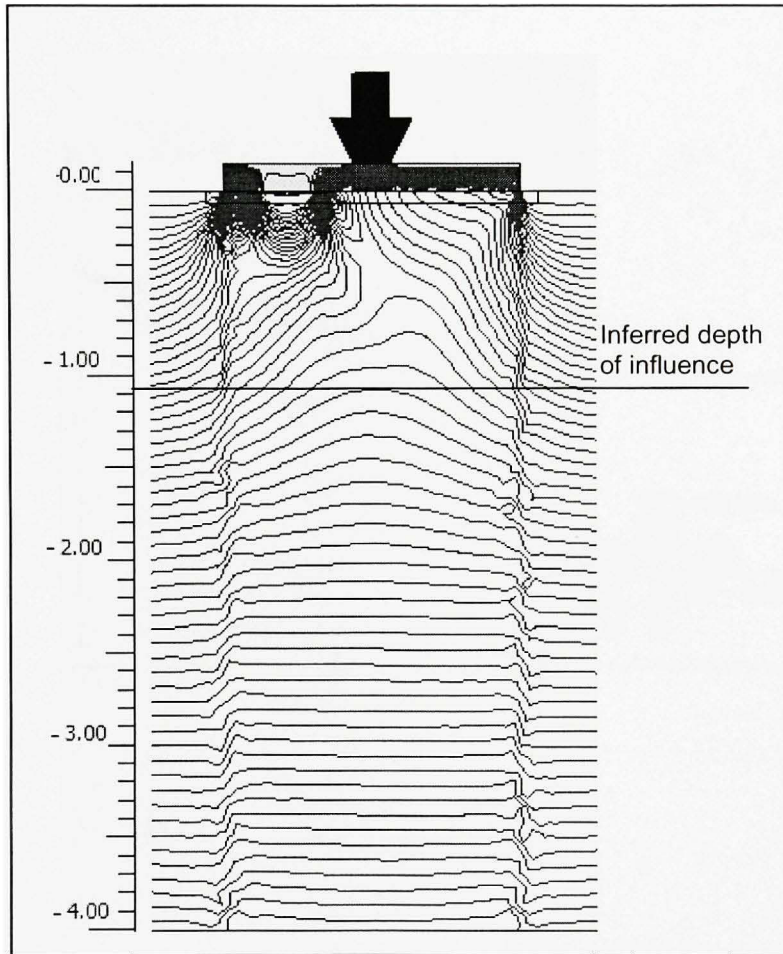
Figure 3.25 *Influence of the off-centered void on the vertical stress distribution.*
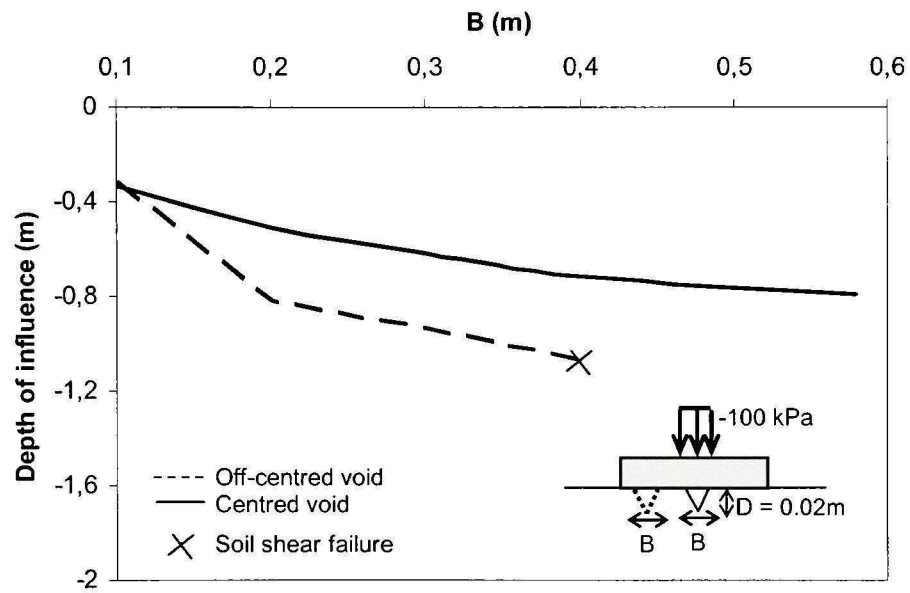
Figure 3.26 *Depth influence under centered and off-centered voids.*
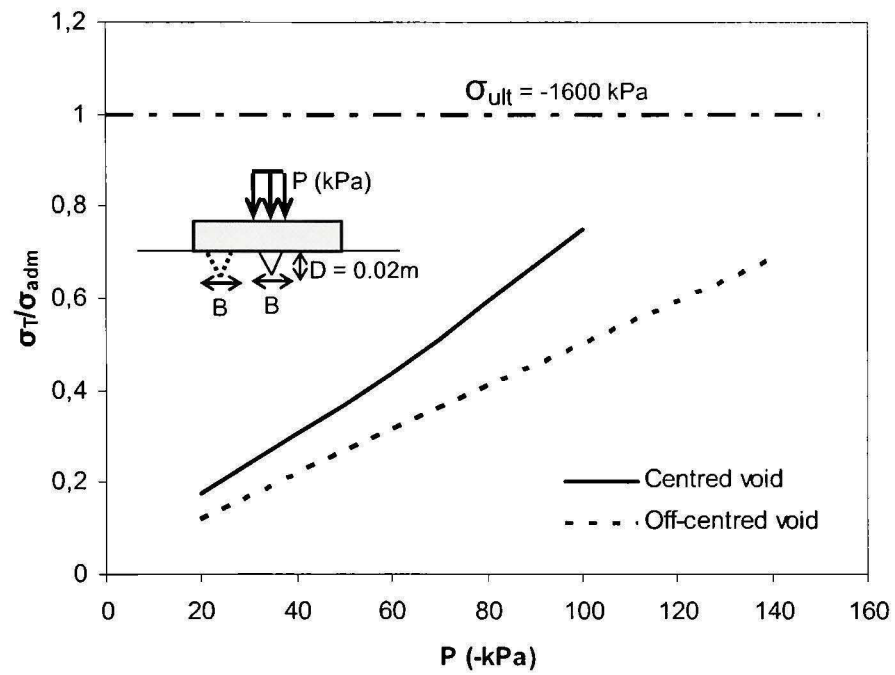
Figure 3.27 *Normalized tensile stresses induced into the concrete slab versus prescribed loads.*

CONCLUSIONS AND RECOMMENDATIONS

Failure of rigid slab-on-grade is usually attributed to two main factors. The first involves aspects related to material failure, which includes fatigue of the concrete and other construction defects. The second category is attributed to the loss of reaction support. Indeed, subsurface soil erosion leads to a contact loss between the slab-on-grade and the supporting soil. A physical model was built to measure the response of the slab-soil system subjected to soil erosion. Parameters such as the settlement profile and the redistribution of the contact pressure under a 1D sand volume loss were measured and used to calibrate a numerical model. A 2D elasto-plastic finite element analysis was then conducted where parameters such as the size of the void underneath the slab, its location, and the magnitude of the load the concrete slab is subjected to were varied. The parameters required for the Hardening Soil Model (Shanz, 1999) used during the numerical analysis are quite simple to estimate and can be easily obtained based on the available literature and soil testing results. The following conclusions can be drawn from this research:

- When the void is centered under the load, the failure of the slab is possible for a certain value of the void width and no soil shear failure was observed. This value is proportional to the external load the slab is subjected to.

- When the void is off centered under the load, shear soil failure may occur around the void before excessive stresses develop in the outer fibers of the slab. Consequently, the slab-on-grade loses its uniform support and becomes unstable, which makes the latter vulnerable under further loading.

The above conclusions are based on limited number of tests under idealized conditions and further experiments and analyses are needed to confirm these findings. Several improvements can be made to the present research:

- Field measurements such as strains and displacements of the concrete slab, and representative voids underneath the slab can be taken over a period of time to validate the full scale numerical results.

- Some hypotheses have been made during the experimental program. The set up can be improved by eliminating one or several of these hypotheses during further experimental investigations. The hypotheses are listed as follow:

- The internal sides of the tank were painted and lined with plastic sheets to reduce friction between the sand and the sides of the tank . The soil lateral boundaries were then supposed to not influence the behavior of the surface structure. A full scale experimental model would be more representative of the real conditions.

- Silica dry sand was used during the experiments. Sand that meets the characteristics described in Section 1.2.2 would be more representative. Capillarity forces due to moisture should also be accounted for.

- Because of laboratory restrictions, the contact pressure was measured at only two symmetrical locations. More points of measurement would give a better calibration of the numerical model.

- The set up built for the experimental program represents a 2D problem (plane strain). The performance of the slab-on-grade subjected to 3D voids needs to be investigated experimentally and numerically.

APPENDIX I

COMPLETE BORINGS LOGS OBTAINED FROM THE CITY OF MONTRÉAL

Because of its format, Appendix I is available on the CD attached.

APPENDIX II

PICTURES OF THE SURVEY

Because of its format, Appendix 2 is available on the CD attached.

APPENDIX III

## SPECIFICATION REPORT RELEASED BY THE CITY OF MONTRÉAL TO THE READY MIXED CONCRETE SUPPLIERS

Because of its format, Appendix 3 is available on the CD attached.

APPENDIX IV

## ILLUSTRATION OF THE EXPERIMENTAL PROCEDURE


Step 1: Filling the container
with sand
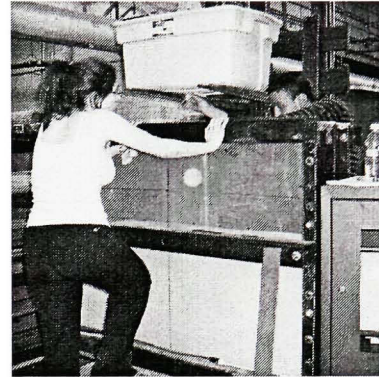
Step 2: Filling the tank from
the container
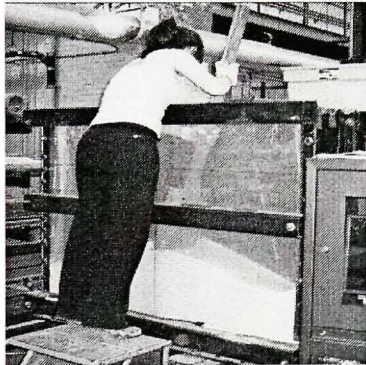
Step 3: Grading a layer of
sand
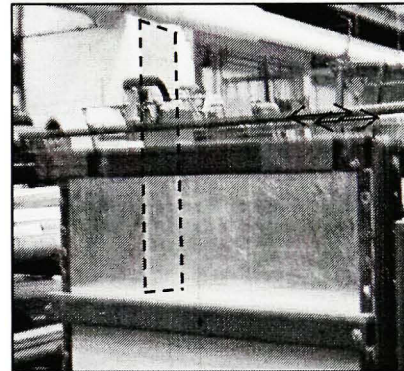
Step 4: Grading the last
layer of sand
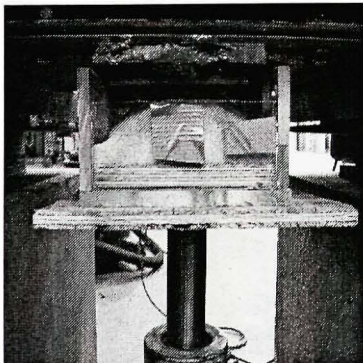
Step 5: Removing 2670 cm^3
from the trap door

REFERENCES

Atkinson, J.H., Brown, E.T., Potts, M., (1975). Collapse of shallow unlined tunnels in dense sand. Tunnels and Tunneling, v 3, pp. 81-87.

Abdulla, W., Goodings, D.J., (1996). Modeling Sinkholes in Weakly Cemented Sand. ASCE Geotechnical Engineering Journal, v 122, No. 12, December, pp. 998-1005.

American Concrete Institute (1995).Building code requirements for structural concrete (ACI 318-95) and commentary (ACI 318-95). Detroit, Mich. : American concrete Institute. 369 p.

Baus, R.L., ASCE, A.M., Wang, M.C., ASCE, M., (1983). Bearing capacity of strip footing above void. Journal of Geotechnical Engineering, v 109, n° 1, Jan, 1983, pp. 1-14.

Brady, B.H.G., Brown, E.T., (1993). Rock mechanics for underground mining. Chapman and Hall, London. 571 p.

Brinkgreve, R., (2001). Plaxis finite element code for soil and rock analyses, Version 8.6. Softwear, Plaxis B V.

Craig, W.H., (1990). Collapse of cohesive overburden following removal of support. Can. Canadian Geotechnical Journal, v 27, pp.355–364.

Chen, F.H., (1988). Foundations on expansive soils. Developments in geotechnical engineering, v 54, Elsevier Science Pub. Co., New York, pp.16.

Davis, E.H., Gunn, M.J., Mair, R. J., Seneviratne, H. N., (1980). The stability of shallow tunnels and underground openings in cohesive material. Geotechnique, v 30, pp. 397-416.

Duncan, J.M., Chang, C., (1970). Nonlinear analysis of stress and strain in soils. Journal of the Soil Mechanics and Foundations Division, ASCE, 96(SM5): pp.1629–1653.

Girould, J.P., (1973). Tables pour le calcul des foundations. v 2, Dunod, Paris, 505 p

Giroud, J.P., Bonaparte, R., Beech, J.F., Gross, B.A., (1990). Design of Soil Layer-Geosynthetic Systems Overlying Voids. Geotextiles and Geomembranes,v 9, pp. 11-50.

Tharp, T.M., (1999). Mechanics of upward propagation of cover-collapse sinkholes. Engineering Geology, v 52, pp. 23-33.

Hauser, E.C., Howell, M.J., (2001). Ground Penetrating Radar Survey to Evaluate Roadway Collapse in Northern Ohio. 2001 Symposium on Application of Geophysics to Environmental and Engineering Problems (SAGEEP), 2001 CD Publication RBA-2, 7 p.

Higawara, T., Grant R.J., Calvello, M., Taylor, R.N., (1999). The effect of overlying strata on the distribution of ground movements induced by tunneling in clay. Soils and foundations, v 39, n°3, pp. 63-73.

Hunt, R.E., (1986). Geotechnical engineering techniques and practices. McGraw-Hill, New York, USA, pp. 643-54.

Jacky, J., (1944). The coefficient of earth pressure at rest. Journal of the Society of Hungarian Engineers and Architects, Budapest, pp. 355–358.

Janbu, J., (1963). Soil compressibility as determined by oedometer and triaxial tests. Proc. ECSMFE Wiesbaden, v 1, pp. 19-25.

Kezdi, A., (1986). Lateral earth pressure. In foundation engineering handbook, ed. H. F. Winterkorn & H. Y. Fang. Van Nostrand Reinhold Co., New York, USA, pp. 216-18.

Kempfert, H.G., Gebreselassie, B., (2006). Excavations and Foundations in Soft Soils. Springer-Verlag, 576 p.

Kemmerly, P.R., (1993). Sinkhole Hazards and Risk Assessment in a Planning Context. American Planning Association. Journal of the American Planning Association, v 59, n°2, pp. 221-229.

Lee, C.J., Wu, B.R., Chen, H.T., Chiang, K.H., (2006). Tunneling stability and arching effects during tunneling in soft clayey soil. Tunneling and Underground Space Technoloy, v 21, n° 2, pp. 119-132.

Material property data, *ASTM A36-Steel plate mechanical properties*, <http://www.matweb.com>. Consulted on December 2007.

Marr, S.A., Gilbert, R.B., Rauch, A.F., (2004). A practical method for predicting expansive soil behavior. Geotechnical Special Publication, n° 126 I, Geotechnical Engineering for Transportation Projects: Proceedings of Geo-Trans 2004, pp. 1144-1152.

Marston, A., Anderson, A.O., (1913). The theory of loads on pipes in ditch and tests of cement and clay drain title and sewer pipe. Iowa State College of Agriculture, 181p

McKelvey III, J. A., (1994). The anatomy of soil arching. Geotextiles and Geomembranes, v 13, n° 5, pp. 317-329.

Newton, J.G., (1984). Review of induced sinkhole development. In: Beck B.F. (ed) Sinkholes: their geology, engineering and environmental impact. Proceedings of the First multidisciplinary Conference on Sinkholes. Balkema, Rotterdam, pp.3-9.

Newton, J.G., Tanner, J.M., Mark, J., (1986). Regional inventory of karst activity in the Valley and Ridge Province, Eastern Tennessee, PHASE I : ORNL/Sub/11-78911/1, OAK Ridge National Laboratory, Oak Ridge, Tennessee. In press.

Newton, J.G., (1987). Review of induced sinkhole. A. A. Balkema, 1984, pp. 3-9.

Plaxis manual, (2001). Material Models Manual. Plaxis BV, Version 8, pp. 5.1-5.14.

Water Research Centre, (1994). Sewerage Rehabilitation Manual – Planning. Medmenham, Marlow, Bucks: WRc, 1994.

Spears, R.E., (1983). Concrete Floors on Ground. Portland Cement Association, Engineering Bulletin, 40 p.

Rowe, P.W., (1962). The stress-dilatancy relation for static equilibrium of an assembly of particles in contact. Proc. Roy. Soc. A. 269, pp.500-527.

Rowe, P.W., (1971). Theoretical meaning and observed values of deformation parameters for soil, in Proc. Of Roscoe memorial symposium, Foulis, Henley-on-Thames, pp. 143-194.

Rajani, B., Zhan, C., (1997). Performance of concrete sidewalks: Field studies. Canadian Journal of Civil Engineering, v 24, n° 2, April, 1997, pp. 303-312.

Rajani, B., (2002). Behavior and Performance of Concrete Sidewalks. Institute for Research in Construction, National Research Council of Canada, Construction Technology Update No. 53, 2002, 4 p.

Sterpi, D., (2003). Effects of the Erosion and Transport of Fine Particles due to Seepage Flow. International Journal of Geomechanics, v 3, n° 1, pp. 111-122.

Skempton, A.W., (1953). The colloidal activity of clays. Proceedings of the 3rd International Conference on Soil Mechanics and Foundation Engineering, Switzerland, v 1, pp. 57-61.

Sharma, J.S., Bolton, M.D., Boyle, R.E., (2001). A new technique for simulation of tunnel excavation in a centrifuge. Geotechnical Testing Journal, v 24, n° 4, pp. 343-349.

Schanz, T., Vermeer, P.A., Bonnier, P.G., (1999). The hardening soil model—Formulation and verification. Proc., Plaxis Symp. Beyond 2000 in Computational Geotechnics, Amsterdam, Balkema, The Netherlands, pp. 281–296.

Therzaghi, K., (1936). Stress distribution in dry and in saturated sand above a yielding trap-door. Proc. Int. Conf. Sil Mechs., v 1, Harvard Univ. Press, Cambridge, MA, 1936, pp. 307-311.

Therzaghi, K., (1943). Theoretical soil mechanics. John Wiley & sons, New York, USA, 66 p.

Waltham, T., Bell, F., Culshaw, M., (2005). Sinkholes and Subsidence- Karst and Cavernous Rocks in Engineering and Construction. Springer, 382 p.

Watson, D.K., Rajapakse, RKND., (2000). Seasonal variation in material properties of a flexible pavement. Canadian Journal of Civil Engineering, v 27, n° 1, pp 44-54.

Wu, B.R., Lee, C.J., (2003). Ground movement and collapse mechanisms induced by tunneling in clayey soil. International Journal of Physical Modeling In Geotechnics. v 3, n° 4, pp. 13-27.